Non-uniform distribution of dendritic nonlinearities differentially engages thalamostriatal and corticostriatal inputs onto cholinergic interneurons

Abbreviated title: Dendritic nonlinearities in striatal cholinergic interneurons

Osnat Oz[1], Lior Matityahu[1], Aviv Mizrahi-Kliger[1,2], Alexander Kaplan[1,2], Noa Berkowitz[1], Lior Tiroshi[1†], Hagai Bergman[1,2,3], Joshua A. Goldberg[1*]

[1]Department of Medical Neurobiology, Institute of Medical Research Israel – Canada, The Faculty of Medicine,
[2]Edmond and Lily Safra Center for Brain Sciences,
The Hebrew University of Jerusalem, 9112102 Jerusalem, Israel
[3]Department of Neurosurgery, Hadassah Medical Center, 9112102 Jerusalem, Israel

[†]Current address: Department of Neurobiology, Northwestern University, Evanston, IL, 60208, USA

[*]Corresponding author, joshua.goldberg2@mail.huji.ac.il

Abstract

The tonic activity of striatal cholinergic interneurons (CINs) is modified differentially by their afferent inputs. Although their unitary synaptic currents are identical, in most CINs cortical inputs onto distal dendrites only weakly entrain them, whereas proximal thalamic inputs trigger abrupt pauses in discharge in response to salient external stimuli. To test whether the dendritic expression of the active conductances that drive autonomous discharge contribute to the CINs' capacity to dissociate cortical from thalamic inputs, we used an optogenetics-based method to quantify dendritic excitability. We found that the persistent sodium (NaP) current gave rise to dendritic boosting, and that the hyperpolarization-activated cyclic nucleotide-gated (HCN) current gave rise to a subhertz membrane resonance. This resonance may underlie our novel finding of an association between CIN pauses and internally-generated slow wave events in sleeping non-human primates. Moreover, our method indicated that dendritic NaP and HCN currents were preferentially expressed in proximal dendrites. We validated the non-uniform distribution of NaP currents pharmacologically; with two-photon imaging of dendritic back-propagating action potentials; and by demonstrating boosting of thalamic, but not cortical, inputs by NaP currents. Thus, the localization of active dendritic conductances in CIN dendrites mirrors the spatial distribution of afferent terminals and may promote their differential responses to thalamic *vs.* cortical inputs.

Introduction

The striatal cholinergic interneuron (CIN) is a key modulator of the striatal microcircuitry, impacting the neuronal excitability, synaptic transmission and synaptic plasticity of spiny projection neurons (SPNs), as well as other striatal interneurons (Abudukeyoumu et al., 2019; Assous, 2021; Goldberg et al., 2012; Matityahu et al., 2022). There are two processes that drive the ongoing release of acetylcholine (ACh) by CINs. First, the two glutamatergic inputs arising from cerebral cortex and intralaminar nuclei of the thalamus can drive CINs to discharge (Bradfield et al., 2013; Ding et al., 2010; Doig et al., 2014; Kosillo et al., 2016; Lapper and Bolam, 1992; Mamaligas et al., 2019; Matsumoto et al., 2001; Sharott et al., 2012; Thomas et al., 2000). While the unitary synaptic currents generated by these two inputs in CINs are identical (Aceves Buendia et al., 2019), thalamic inputs to CINs dominate in the sense that they that give rise to larger excitatory post-synaptic potentials (EPSPs) in acute striatal slices (Johansson and Silberberg, 2020) and can trigger abrupt pause responses, often flanked by excitatory peaks, to external saliency-related cues (Apicella et al., 1991; Goldberg and Reynolds, 2011; Graybiel et al., 1994; Kimura et al., 1984; Matsumoto et al., 2001; Morris et al., 2004; Raz et al., 1996). In contrast, cortical inputs to CINs are weaker in that, in acute striatal slices, they give rise to smaller EPSPs in most CINs (Mamaligas et al., 2019) and cannot trigger the pause response (Ding et al., 2010), although, these differences are less pronounced in intact animals (Doig et al., 2014).

Second, even in the absence of afferent input, CINs exhibit multiple autonomously generated discharge patterns – including regular and irregular pacemaking, as well as burst firing (Bennett et al., 2000; Bennett and Wilson, 1999; Goldberg and Reynolds, 2011; Goldberg and Wilson, 2010). These firing patterns are generated by an interplay between various nonlinear ionic currents including voltage- and calcium-activated K^+ currents, as well as two voltage-dependent pacemaker currents: the hyperpolarization-activated cyclic nucleotide-gated (HCN) current; and the persistent Na^+ (NaP) current (Bennett et al., 2000; Deng et al., 2007; Goldberg et al., 2009; Goldberg and Wilson, 2010, 2005; McGuirt et al., 2021; Oswald et al., 2009; Song and Surmeier, 1996; Wilson, 2005; Wilson and Goldberg, 2006). The main purpose of these pacemaker currents presumably is to guarantee the ongoing release of ACh onto the striatal microcircuitry by sustaining the autonomous discharge of CINs. Nevertheless, these pacemaker (and other subthreshold) currents will also impact how cortical and thalamic inputs are integrated by the CINs.

Attaining a mechanistic (e.g., dynamical systems) understanding of how the repertoire of CIN firing patterns is generated, requires a full characterization of the nonlinear properties of the pacemaker (and other) currents (e.g., by determining their voltage dependence and kinetics) – which is a daunting endeavor. In contrast, understanding how these currents impact synaptic inputs is a simpler task. Because individual synaptic inputs are small, the membrane nonlinearities can be *linearized* making the analysis of their impact simpler and more general – a treatment called the quasi-linear membrane approximation. This analysis dates back to Mauro (Koch, 1984; Mauro et al., 1970) and has shown that quasi-linear membranes can give rise to two qualitatively different transformations of inputs: *amplification* and *resonance* (Goldberg et al., 2007; Hutcheon and Yarom, 2000). Being a linear approximation, the quasi-linear approximation is amenable to Fourier analysis, which helps to better define these transformations as linear (time-invariant) filters on the input in frequency space.

Amplification arises from regenerative ionic currents – that provide positive feedback – including inward (depolarizing) currents activated by depolarization, such as the NaP current. Here the main effect in frequency space is amplification of the amplitude response (as compared to the response of a passive linear membrane). Resonance arises from restorative currents – that provide negative feedback – including inward currents activated by hyperpolarization, such the HCN current. In frequency space, the defining properties of resonance is a peak (at a non-zero frequency) in the amplitude response, and a zero-crossing of the phase delay (at a nearby frequency). On a practical level, the quasi-linear response properties of a membrane can be measured by providing a small-amplitude, sinusoidally-modulated voltage command to an intracellularly-recorded neuron and recording the resultant sinusoidal output current. Calculating the ratio of the voltage amplitude to the current response yields an estimate of the membrane's impedance (which is, loosely speaking, an indication of the neuron's "input resistance" to a sinusoidal input as a function of its frequency). Membrane impedances have been reported for various neuronal types in the brain (Hutcheon et al., 1996; Ulrich, 2002), including in the striatum (Beatty et al., 2015). Beatty and collaborators (2015) found that CINs exhibit a resonance in the vicinity of 1 Hz. Moreover, they found that the shape of the impedance function depended on the holding voltage, which is understandable given that the amplitude of the various subthreshold currents is voltage-dependent. Finally, with use of tetrodotoxin (TTX), a selective antagonist

101 of voltage-activated Na^+ (Nav) channels, Beatty and collaborators (2015) demonstrated that
102 NaP currents contributed to these filtering properties of the CIN membrane.

103 Use of somatic voltage perturbations, however, fails to discriminate the role played by
104 the CINs' dendritic arbor *per se* in transforming synaptic inputs. The CINs' dendritic arbor
105 can span well over half a millimeter from the soma (Wilson, 2004), with cortical inputs
106 terminating on distal dendrites and thalamic inputs terminating perisomatically and on
107 proximal dendrites (Doig et al., 2014; Lapper and Bolam, 1992; Mamaligas et al., 2019;
108 Thomas et al., 2000). Both dendritic morphology (as taught by cable theory) and dendritic
109 nonlinearities will lead to distal cortical inputs being integrated differently from proximal
110 thalamic input. Thus, the impact of membrane nonlinearities on the quasi-linear
111 approximation will depend on *where* they are expressed throughout the dendritic arbor. To
112 address this question, we recently developed an optogenetics-based experimental method
113 (that relies on the use of quasi-linear cable theory and Fourier analysis) to determine the
114 duration of the delays introduced by dendrites, and how these delays impact the rapidity and
115 fidelity of a neuron's response to its input. We used our method to study GABAergic neurons
116 of the substantia nigra pars reticulata (SNr) that expressed channelrhodopsin-2 (ChR2). We
117 illuminated (with a 470 nm LED) either a small perisomatic region or the entire dendritic
118 arbor. Comparison of the two illumination regimes enabled us to demonstrate that dendrites
119 (that in the SNr can be >700 μm long) introduce a significant integration delay. The analysis
120 also yielded that SNr dendrites behaved like passive linear filters, without evidence for
121 amplification or resonances, or any dependence on holding voltage (Tiroshi and Goldberg,
122 2019).

123 In the present study, we apply our method to study nonlinearities of CIN dendrites.
124 We demonstrate that HCN and NaP currents shape the quasi-linear response properties of
125 CINs, and that dendrites contribute additional phase delays. Furthermore, we show that our
126 analysis can reveal information about dendritic location of membrane nonlinearities, and use
127 the analysis to deduce that both HCN and NaP currents are expressed primarily proximally.
128 Blocking NaP currents pharmacologically revealed that only perisomatic illumination triggers
129 a boosting response. The proximal distribution of NaP currents is further supported by
130 measuring: a) how far autonomously generated backpropagating action potentials (bAPs)
131 actively invade the dendritic arbor; and b) the differential boosting by NaP currents of
132 proximal thalamostriatal vs. distal corticostriatal EPSPs.

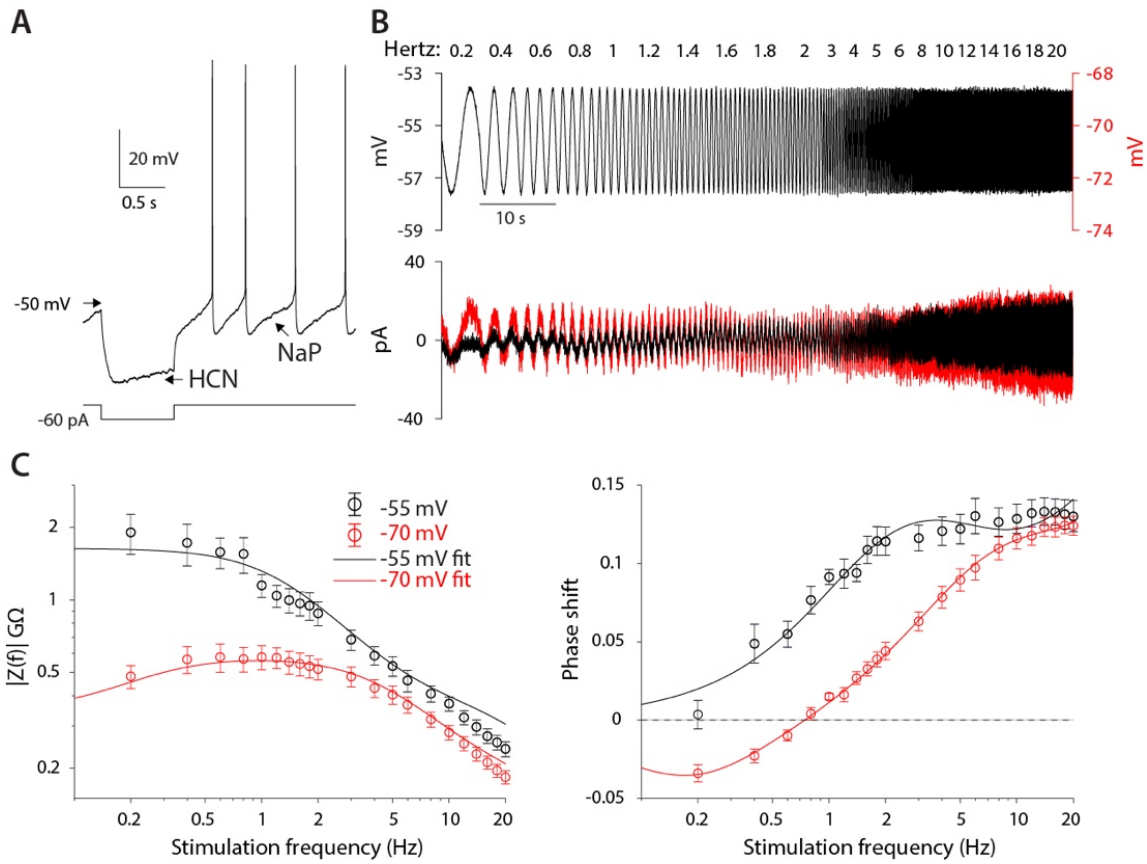

Figure 1: CIN membranes exhibit voltage-dependent quasi-linear properties. **A.** CINs exhibit a voltage sag due to HCN currents, and autonomous pacemaking due to NaP currents. **B.** Application of 2 mV sinusoidal voltage commands to the soma, of increasing frequencies, elicits a current response that is voltage dependent (black trace, –55 mV; red trace, –70 mV). **C.** Estimation of the impedance (left) and phase shift (right) show that at –55 mV, CINs exhibit an amplified impedance and that at –70 mV, CINs exhibit a resonance (non-monotonic impedance and negative phase delays). Solid lines are parameter fits for $(\alpha^2 + \beta^2)^{-1/2}$ up to a scale factor (left), and phase shift, ϕ_s (right, see Eq. 5).

Results

Ionic currents underlying amplification and resonance in cholinergic interneurons

The HCN and NaP currents depolarize CINs over largely non-overlapping voltage ranges. The HCN current is mostly active below –60 mV and is responsible for the voltage sag in response to a hyperpolarizing current pulse (Figure 1A, "HCN"), whereas the NaP current takes over at –60 mV and is necessary and sufficient (Bennett et al., 2000) to drive CINs to action potential threshold (Figure 1A, "NaP"). Therefore, because NaP is a regenerative current, while HCN is a restorative current, we would expect the current responses to an oscillating voltage command to depend strongly on whether the membrane voltage is clamped above or below –60 mV (Beatty et al., 2015). We therefore held mouse CINs in whole-cell voltage clamp (*n = 10* neurons, *N = 4* mice), first at –55 mV, and

144 subjected them to a voltage command that was composed of a continuous sequence of
145 sinusoidal cycles with an amplitude of 2 mV and a frequency that increases discretely from
146 0.2 to 20 Hz. The current amplitude was very small at low frequencies and increased
147 monotonically to the high frequency (Figure 1B, black), which is suggestive of an impedance
148 curve with amplified lower frequencies. Loosely speaking, this means that the CINs' "input
149 resistance" to a low frequency oscillatory input currents is boosted. As expected (Figure 1C,
150 black), the impedance curve, $|Z(f)|$, exhibited an amplifying structure, with the phase delay
151 being strictly positive. In order to quantify the degree of amplification, we fit the model of
152 the phase delay, ϕ_s, for an iso-potential cell with quasi-linear properties (see Materials and
153 Methods). In this fit, there is a (negative) amplifying parameter, μ_n – that is derived from
154 biophysical properties of amplifying current (e.g., the slope of the activation curve, reversal
155 potential, etc.) (Goldberg et al., 2007) – which was estimated to be $\mu_n = -3.9$.

156 When neurons were held at –70 mV ($n = 10$ neurons, $N = 7$ mice), the current
157 response was very different, it was much larger at subhertz frequencies as compared to the
158 experiment at –55 mV, and then exhibited what looks like a slightly decreasing amplitude for
159 frequencies near 1 Hz, followed by an amplitude increase at higher frequencies (Figure 1B,
160 red). Estimation of the amplitude response and phase delay (Figure 1C, red), revealed
161 significantly different curves (amplitude: $P = 6{\cdot}10^{-25}$, phase: $P = 1{\cdot}10^{-17}$, ANCOVA) with a
162 clear resonance peak at approximately 1 Hz, and a zero crossing at a slightly lower frequency
163 (Figure 1C, red). Fitting the somatic phase delay yielded a reasonable fit only when both an
164 amplifying and resonant component were included in the fit with the amplifying parameter
165 ($\mu_n = -3.4$) being only slightly reduced relative to the –55 mV fit. In contrast, the additional
166 (positive) resonance parameter, μ_h – which is derived from the biophysical properties of the
167 restorative current – was estimated to be $\mu_h = 1.6$ (see Materials and Methods) based on the
168 fit to the negative lobe in the phase delay.

169 The previous experiments suggest that the amplifying effect at –55 mV occurs due to
170 prominence of the amplifying NaP current in that voltage range, whereas the resonance
171 visible at –70 mV is due to the HCN current that dominates that voltage range. This
172 conclusion was supported by the fact that application of 1 μM TTX ($n = 9$ neurons, $N = 4$
173 mice), that abolished autonomous spiking and slightly hyperpolarized the CIN (Figure 2A),
174 reduced the impedance ($P = 9{\cdot}10^{-9}$) and exhibited a trend toward a shortened phase delay (P
175 $= 0.137$, ANCOVA, Figure 2B). These changes are captured by the amplification parameter
176 being estimated as less negative ($\mu_n = -2.0$), which reduces ϕ_s (Eq. 5 in Materials and

Methods). Similarly, application of 10 µM ZD7288, the selective HCN antagonist ($n = 9$ neurons, $N = 7$ mice), which abolished the sag response (Figure 2C), abolished the resonance peak in the impedance curve ($P = 4{\cdot}10^{-16}$) and significantly reduced the negative lobe in the phase delay ($P = 0.018$, ANCOVA, Figure 2D), which was captured by the resonance parameter being reduced to $\mu_h = 0.5$.

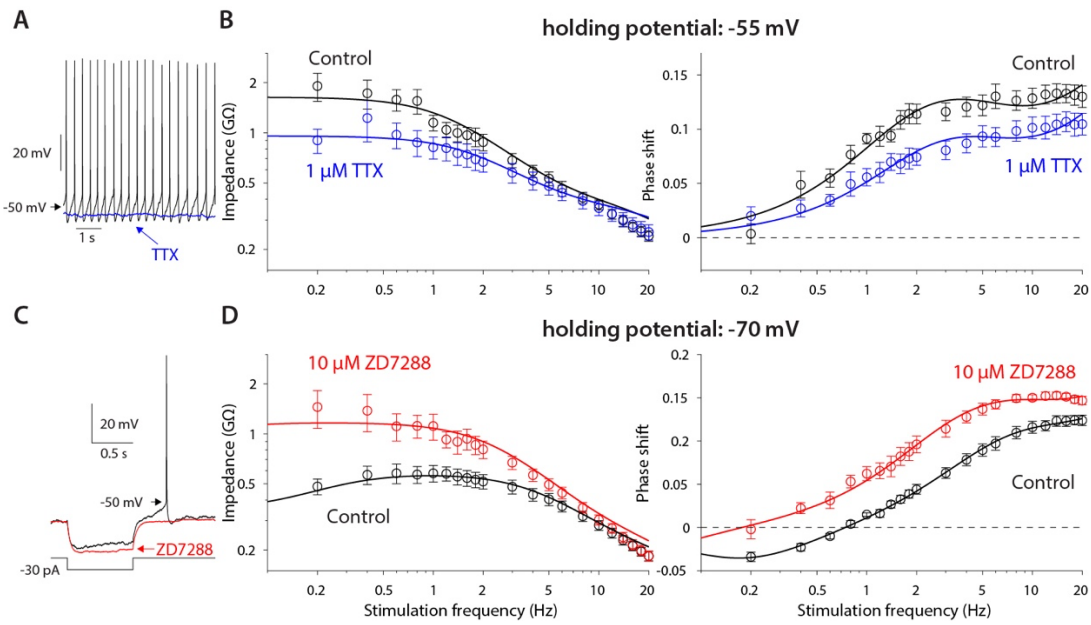

Figure 2: Amplification is caused by NaP currents, whereas the resonance is caused by HCN currents. A. TTX (blue) prevents autonomous spiking (black). **B.** TTX prevents amplification of the impedance (left), and reduces the phase shift (right). **C.** ZD7288 (red) abolishes the voltage sag (black). **D.** ZD7288 abolishes the resonance peak in the impedance, and the negative phase shifts in the subhertz range. Solid lines are parameter fits as in Figure 1.

<u>Optogenetic interrogation of the spatial distribution of NaP and HCN currents in the CIN dendritic arbor</u>

While the above experiments demonstrate the NaP and HCN currents are capable of transforming subthreshold voltage fluctuations, the question remains as to where within the CIN's somatodendritic compartments these currents perform their amplifying and restorative actions, respectively. One extreme scenario is that they are restricted to the axosomatic region (where they are needed for sustaining the autonomous firing patterns of the CINs). In that scenario, the dendrites could be entirely linear, passively transmitting the distal depolarizations to the soma. Only at the soma are the inputs then transformed by these currents. However, a more realistic scenario is that these currents are also expressed dendritically and exert their nonlinear influence on synaptic inputs more distally. But in this scenario, we would still want to know where along the dendrites the currents are expressed.

194 To determine the precise location of these channels would require advanced *in situ* molecular
195 and anatomical techniques and/or direct electrophysiological recordings from CIN dendrites
196 in conjunction with advanced imaging techniques. While these experiments may, in principle,
197 be done, we wondered whether the optogenetics-based technique that we recently developed
198 to interrogate the role of dendrites in synaptic integration (Tiroshi and Goldberg, 2019) could
199 help us address this question.

200 We previously showed that the impact of dendrites on synaptic integration can be
201 quantified by studying the response of neurons that express ChR2 post-synaptically to (470
202 nm) illumination of their dendritic arbor. In particular, we compared between two spatial
203 patterns of illumination of the somatodendritc arbor of SNr neurons: either a small
204 perisomatic region (approximately 100 µm in diameter) or the entire dendritic arbor. By
205 using sinusoidally-modulated blue LED illumination at various temporal frequencies, we
206 were able to calculate the phase delays produced by both spatial patterns, and found that
207 illumination of the entire dendritic arbor introduced larger phase delays. In order to quantify
208 the effect, we fit the data to a tractable theoretical model of a semi-infinite cable (Goldberg et
209 al., 2007; Tiroshi and Goldberg, 2019). As mentioned above, in the case of the SNr neuron,
210 we found that the dendrites were well-fit by a passive linear cable model, whose parameters
211 (i.e., time and space constants) we could estimate. The conclusion that SNr dendrites were
212 largely linear was further supported by the finding that these phase delays were voltage-
213 independent (Tiroshi and Goldberg, 2019).

214 Because CINs exhibit prominent amplifying and resonating currents that are strongly
215 voltage dependent (Figures 1&2), we posited that by using the same optogenetic technique
216 and semi-infinite cable model we would be able to quantify the contribution of CIN dendrites
217 to post-synaptic integration. In particular, we hypothesized that by fitting a *quasi-linear* cable
218 model, we would be able to quantify to what degree CIN dendrites *per se* possess amplifying
219 or resonating properties (See Materials and Methods). Finally, by comparing illumination of
220 the proximal *vs.* the entire dendritic arbor, we could learn something about the localization of
221 the nonlinearities along the dendritic arbor. To this end, we crossed mice that express Cre-
222 recombinase under a ChAT promoter with the Ai32 mouse that expresses ChR2 and EYFP in
223 a Cre-dependent manner (see Materials and Methods). The cholinergic neuropil and
224 individual CINs could be clearly visualized in the dorsal striatum of these ChAT-ChR2 mice
225 (Figure 3A). Individual CINs were patched and recorded in voltage clamp, while illuminating

226 either the proximal region with a 60X water-immersion objective (Figure 3A) or the entire
227 slice with a 5X air objective, with a continuous sequence of sinusoidally modulated
228 illumination waveforms at various frequencies (Figure 3B, blue).

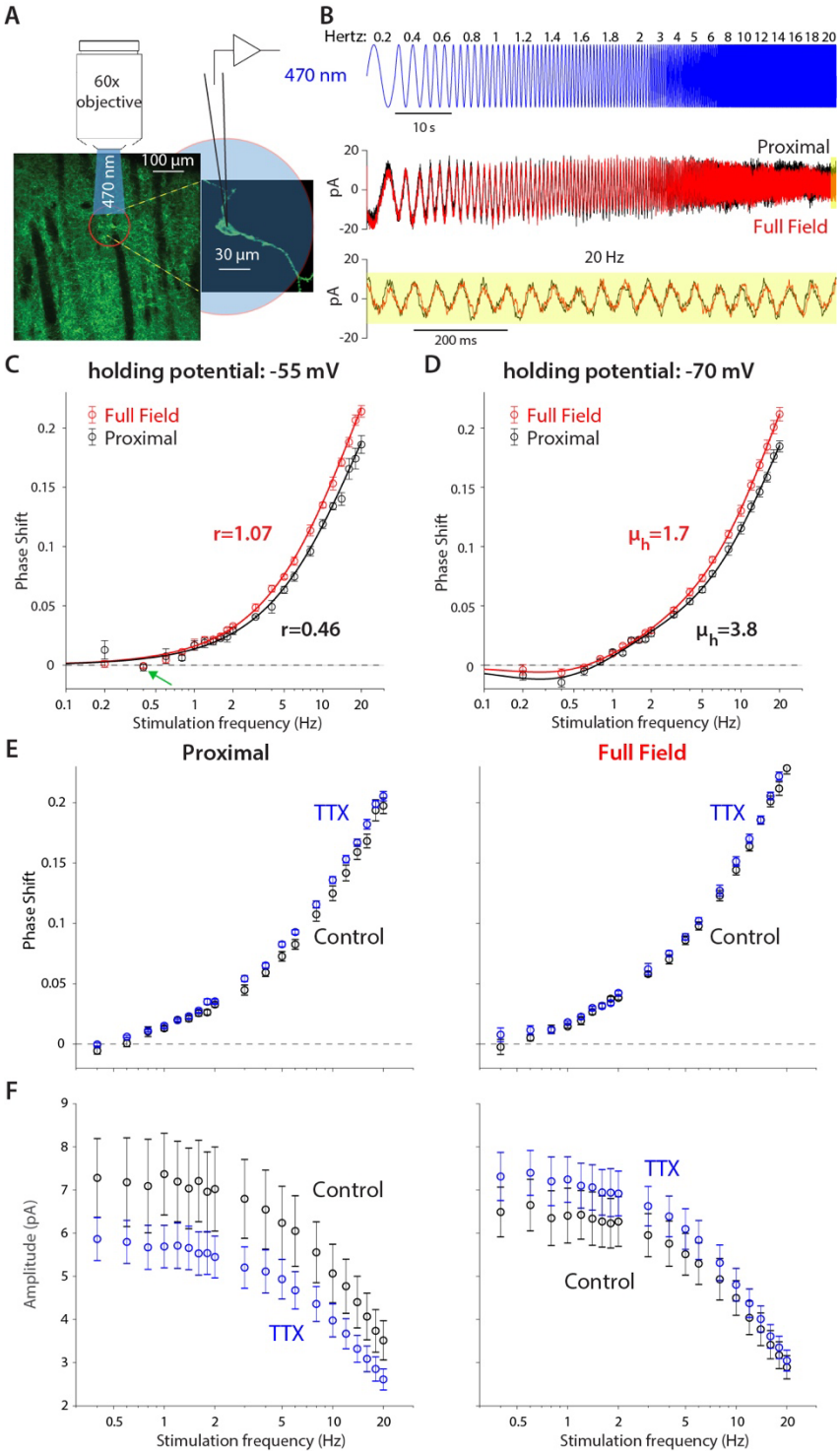

Figure 3: Optogenetic interrogation of the quasi-linear properties of CIN dendrites indicates that dendritic nonlinearities are more prominent proximally. A. A CIN in a sagittal slice from ChAT-ChR2 mouse is patch-clamped in the whole-cell mode while either a small proximal region around the soma or the full-field are illuminated with a sinusoidally modulated 470 nm LED. **B.** The current response to the proximal (black) and full-field (red) illumination differ, with the phase of the full-field illumination right-shifted at the higher frequencies (20 Hz is highlighted in yellow). **C.** Phase shifts at –55 mV holding potential, calculated for proximal (black) and full-field illumination (red). A tendency towards negative phase shifts is present at 0.4 Hz (green arrow). Fitting the passive model at –55 mV demonstrated that the effective range of illumination (r) is larger for the full field fit (Eq. 2). **D.** Phase shifts at –70 mV holding potential, exhibit a negative phase shift, and the resonance parameter (μ_h) is smaller for the full field fit, as is the magnitude of the amplification parameter (μ_n, see main text). The elevation in these parameters' magnitudes when illuminating proximally relative to full-field suggest that the surface densities of NaP and HCN currents is higher proximally. **E.** Phase response for proximal (left) and full-field illumination (right) in TTX at –55 mV. **F.** Amplitude response for proximal (left) and full-field illumination (right) at –55 mV reveals an opposite effect of TTX.

229 Comparison of the somatic current traces in response to proximal (Figure 3B, black)
230 *vs.* full-field (red) illumination demonstrated that the phase of the full-field-generated current
231 is delayed relative to the proximally-generated current. This could be observed in the raw
232 data both for the low and high (yellow inset) frequencies. The effect at the high frequency
233 was very evident when plotting the phase delay curves both when the CINs were held at –55
234 mV (Figure 3C) and at –70 mV (Figure 3D). Estimation of these phase delays revealed
235 delays that were considerably larger than those observed with the electrical somatic
236 stimulation (Figure 1). The main contributor to the large delays are the kinetics of the ChR2,
237 ϕ_C (Eq. 6b, in Materials and Methods) with an additional dendritic delay ϕ_d (Eq. 2 in
238 Materials and Methods). So we used independent measurements of the ChR2 kinetics in
239 CINs (Figure 3–figure supplement 1), and previous literature about these kinetics (Nagel et
240 al., 2003; Tchumatchenko et al., 2013) to fit the phase and amplitude contribution of ChR2,
241 as explained in Appendix 1.

242 We found that fitting our model of ChR2 kinetics to the significantly-different phases
243 observed in the proximal and full-field illuminations at – 55 mV ($n = 5$ neurons, $N = 4$ mice,
244 $P = 4 \cdot 10^{-3}$, ANCOVA) yielded that the full-field illumination activated roughly twice the
245 electrotonic range ($r = 1.07$) that was activated by the proximal illumination ($r = 0.46$,
246 Figure 3C). However, a closer look at these fits reveals that the phase delay at 0.4 Hz (for
247 both the proximal and full field illumination), is not captured by this model. This dip in phase
248 delay (Figure 3C, green arrow) at this low frequency is reminiscent of what a restorative
249 current is expected to do. In order to accentuate the effect of the restorative HCN currents, we
250 repeated the experiment at the –70 mV holding potential (Figure 3D). In this case ($n = 14$
251 neurons, $N = 10$ mice), the phase delays at the lower frequencies (especially at 0.4 Hz) were

negative, which was reminiscent of the results from the electrical voltage stimulation experiments (Figure 1) at the –70 mV holding potential. Estimation of the amplitude responses for proximal and distal stimulation at both holding potentials revealed that they were less sensitive at revealing the resonance structure (Figure 3–figure supplement 2), that was more readily read off from the phase responses (Figure 3D) in the sense that phase estimates provided tighter error bars than the amplitude estimates.

When fitting a full ChR2 kinetics plus quasi-linear dendrite model (incorporating both amplifying and restorative parameters) to the –70 mV measurements (Figure 3D), we found that the curves were significantly different ($P = 8 \cdot 10^{-4}$, ANCOVA) and the estimates of the effective electrotonic range of illumination remained similar to those estimate with the passive model (Figure 3C): $r = 1.06$ for the full-field and $r = 0.58$ for the proximal illumination. Here too the restorative parameter was estimated to be larger for the proximal fit ($\mu_h = 3.4$) relative to the full field fit ($\mu_h = 1.7$), suggesting that the HCN currents are denser more proximally.

Table 1 summarizes the model parameters used to fit the curves in Figures 1-3. In Appendix 1, we discuss how the various parameters affect the model and provide a more detailed description of how the parameter space was searched to fit the model.

Figure, Curve	μ_n	μ_h	τ_n (ms)	τ_h (ms)	γ_R	τ (ms)	r	Amp (GΩ)
1C, -55 mV	-3.9189	-	28	-	5.4296	41.8	-	2.4728
1C, -70 mV	-3.3854	1.5863	11.6	1077.8	5.8722	26.1	-	1.4229
2B, TTX	-2.0178	-	31.7	-	3.4610	19.4	-	1.3809
2B, ZD7288	-1.8988	0.4844	13.4	9107.5	2.6111	17.2	-	0.8323
3C, proximal	-	-	-	-	-	35.8	0.4360	-
3C, distal	-	-	-	-	-	26.8	1.0651	-
3D, proximal	-1.4763	3.4400	60.0	551.2	3.3405	33.6	0.5788	-
3D, distal	-0.8885	1.6646	49.2	403.3	3.8850	45.3	1.0646	-

Table 1. Parameters fit to quasilinear model in Figures 1–3.

The conclusion that the HCN current is concentrated proximally is buttressed by the fact that the negative phase delays in the subhertz frequency range tended to be less negative for the full-field illumination ($P = 0.037$, Wilcoxon rank sum test on phase delays at 0.4 Hz). In the framework of our quasi-linear model, the only mathematically possible way to recreate this finding while increasing the effective electrotonic range r being illuminated is by reducing the restorative parameter μ_h. Otherwise, if μ_h were constant then illuminating a larger region of the cable – by increasing r – would necessarily recruit more restorative current, thereby making the negative delays more negative (See Appendix 1).

Aside from the deviation at 0.4 Hz (Figure 3C, green arrow, which may be indicative of a resonant component), the other phase measurements at –55 mV are consistent with a simple model of ChR2 kinetics plus a passive dendritic delay, thereby raising the possibility that optogenetic dendritic activation fails to engage NaP currents. This failure could suggest that NaP currents are relatively absent from the dendrites. However, our somatic measurements showed clear evidence that NaP currents affect the quasi-linear properties of the soma (Figure 2B). Additionally, the fit to the phases at –70 mV, required the inclusion of an amplification parameter, which was estimated to have a larger magnitude for the proximal illumination ($\mu_n = -1.5$) than for the full-field illumination ($\mu_n = -0.9$). It therefore seems more likely that the Nav channels that underlie the NaP currents are localized proximally and taper off distally. To test this, we repeated the measurements at –55 mV before and after application of TTX. While TTX application may have slightly increased the phase delays for both proximal and full-field illumination (Figure 3E) – which could reflect a reduction in the overall dendritic membrane conductance of the CINs, and therefore a lengthening of its space constant – the amplitude responses (Figure 3F) unequivocally show that TTX exerts an *opposite* affect when proximal *vs.* full-field illumination are used. While full-field illumination in TTX increased the somatic current's amplitude response (control: $n = 9$ neurons, $N = 7$ mice; TTX: $n = 14$ neurons, $N = 8$ mice, $P = 7 \cdot 10^{-9}$, ANCOVA) presumably by reducing the current escape via the dendritic membrane, proximal illumination in TTX reduced the somatic current's amplitude response (control: $n = 9$ neurons, $N = 7$ mice; TTX: $n = 12$ neurons, $N = 6$ mice, $P = 1.1 \cdot 10^{-4}$, ANCOVA) indicating that proximal NaP currents indeed boost the somatic current, as concluded from the somatic experiments (Figure 2). Thus, this pharmacological result provides *model-independent* evidence that the NaP currents are expressed primarily proximally and less so distally. In the following section, we provide independent evidence in support of this conclusion.

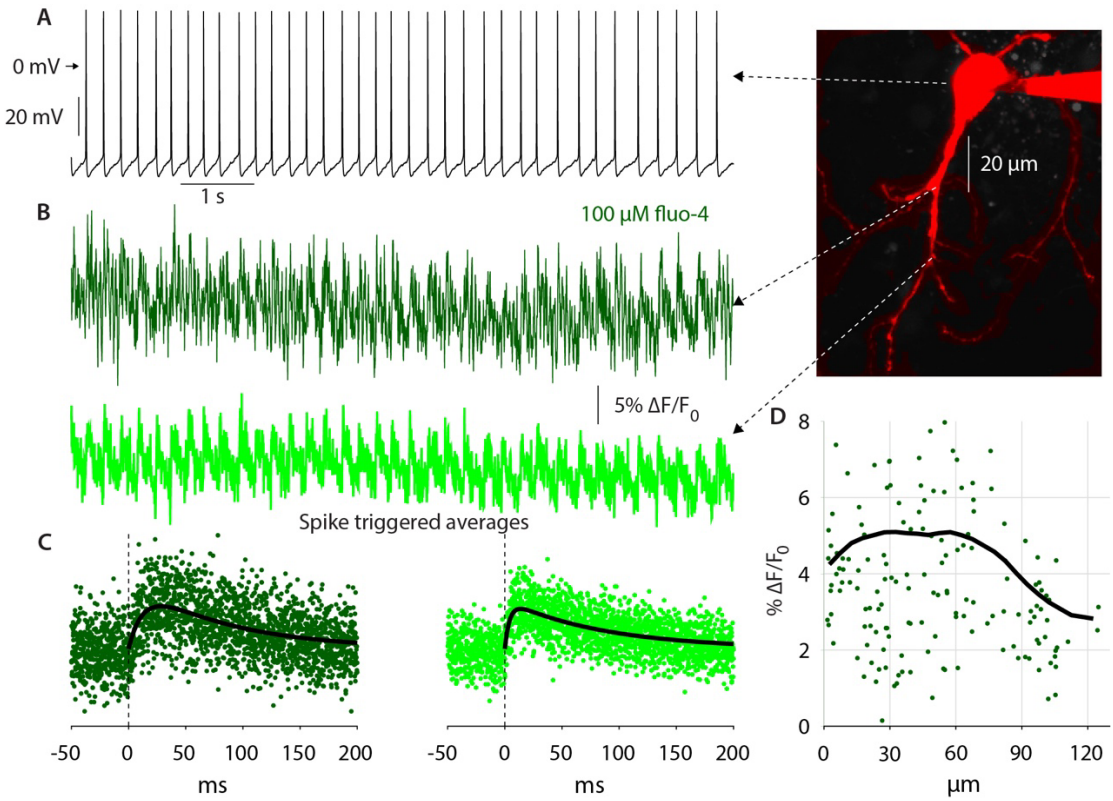

Figure 4: Autonomous action potentials actively back-propagate in CIN dendrites up to 70 µm from the soma. A. Autonomous discharge of a CIN that was patched and filled with fluo-4 and Alexa Fluor 568 for 2PLSM imaging (image). **B.** Line scans at various distances from the soma exhibit Ca^{2+} oscillations caused by bAPs. **C.** Calculating the spike-triggered average of these oscillations and fitting an alpha-function gives an estimate of the amplitude of these oscillations (in % $\Delta F/F_o$). **D.** The scatter plot of these amplitudes as a function of distance from the soma (11 CINs from 7 mice are pooled) exhibits a large degree of variability. However, a 35 µm moving average (black line) exhibits that the Ca^{2+} transients begin to decay approximately 70 µm from the soma, indicating that bAPs are supported by Nav channels up to that point (the initial increase up to 20 µm is due to the increase in the surface-to-volume ratio in the large proximal dendrites).

302 <u>Distance of dendritic bAP invasion indicates location of amplifying Nav channels</u>

303 The persistent and fast-inactivating Nav currents flow through the same Nav channels
304 (Alzheimer et al., 1993). Therefore, a method that is indicative of where these NaV channels
305 are located will indicate where the NaP current can be found. One such method involves
306 determining to what distance from the soma dendritic bAPs invade the dendritic arbor. To
307 this end, we used 2PLSM Ca^{2+} imaging to measure the size of the Ca^{2+} transients elicited by
308 bAPs in autonomously firing CINs at various distances from the soma (Figure 4A). We
309 conducted line scans ($n = 11$ neurons, $N = 7$ mice) to measure the Ca^{2+} signals at various
310 distances from the soma (Figure 4B). Next, we estimated the size of the spike triggered
311 average (STA) of the $\Delta F/F_0$ Ca^{2+} signal, by averaging around spontaneous APs measured at
312 the soma (Figure 4C). The amplitude of the STA was estimated by fitting it with an alpha-
313 function (see Materials and Methods). A scatter plot of STA amplitude *vs.* distance from

314 soma demonstrates a large degree of variability (Figure 4D). Nevertheless, applying a 35 µm
315 moving average to the scatter plot reveals a trapezoidal dependence of Ca^{2+} transient sizes
316 (Figure 4D, black). We previously demonstrated that somatic Ca^{2+} transients are smaller than
317 dendritic transients due to the difference in the surface-area-to-volume ratio (Goldberg et al.,
318 2009; Rehani et al., 2019). In the same vein, the initial dip in the size of the transients at short
319 distances from the soma result from the large size of the proximal dendrites (Figure 4D),
320 relative to the distal dendrites. Neglecting that effect, we found that the size of the bAP-
321 driven Ca^{2+} transients remains constant up to approximately 70 µm from the soma, and then
322 drops off. Additionally, in 7 CINs ($N = 5$ mice) in which we had measurements of $\Delta F/F_0$ at
323 both proximal and distal (>70 µm) locations, we found that the median distal signal was
324 significantly lower than the proximal one by 29% ($P = 0.047$, Wilcoxon rank sum test). This
325 spatial dependence of the Ca^{2+} transient amplitude, suggests that the bAP maintains a
326 constant amplitude due to the presence of Nav channels that sustain their regenerative nature
327 out to some 70 µm from the soma. Farther out the Ca^{2+} transients decrease presumably due to
328 a drop off in Nav channel expression, which leads to a lower amplitude bAPs, and hence less
329 Ca^{2+} via voltage-activated Ca^{2+} channels. Thus, this measurement strengthens the conclusion
330 that NaP currents are present in CIN dendrites – primarily in proximal dendrites (up to
331 approximately 70 µm from the soma).

332 <u>NaP currents boost proximal thalamic inputs but not distal cortical inputs to CINs</u>

333 The above data indicate that Nav channels are preferentially expressed in proximal
334 dendrites. These channels should amplify synaptic inputs impinging on the dendrites. In the
335 case of linear dendrites – either passive or even quasi-linear dendrites – the relative boosting
336 will affect all inputs at all locations equally. However, as demonstrated in Appendix 2 – using
337 a simulated nonlinear dendrite that expresses the NaP current proximally – proximal inputs
338 are more strongly *nonlinearly* boosted than distal inputs, because the latter decay passively
339 before reaching the amplifying region, and are therefore boosted less.. Thus, because
340 thalamic inputs on to CINs terminate proximally, whereas cortical inputs terminate distally
341 (Doig et al., 2014; Lapper and Bolam, 1992; Mamaligas et al., 2019; Thomas et al., 2000), in
342 order to generate comparable EPSPs we presumably need to activate many more distal
343 cortical inputs than proximal thalamic inputs. However, because distal cortical inputs are
344 presumably amplified less their spatial summation at the soma will also be amplified less. In
345 contrast, because proximal thalamic inputs consist of individual inputs, each of which

346 engages the local nonlinear amplification, their summation at the soma will also exhibit more
347 amplification. Thus, we expect only the thalamic – but not cortical – inputs to be significantly
348 boosted by Nav current. To test this, we transcranially inoculated the parafascicular nucleus
349 (PfN) of Vglut2-ires-Cre mice with adeno-associated viruses (AAVs) harboring Cre-
350 dependent ChR2 and EYFP genes (Figure 5A) (Aceves Buendia et al., 2019; Rehani et al.,
351 2019). Two weeks later, we tested the sensitivity of optogenetically-evoked monosynaptic
352 EPSPs (Figure 5–figure supplement 1A) to ranolazine (30 μM), a selective antagonist of the
353 NaP current, in CINs patched in acute striatal slices. The mean amplitude of the EPSP was
354 reduced by a median of 16% ($n = 11$ neurons, $N = 4$ mice, $P = 0.04$, Wilcoxon signed-rank
355 test, Figure 5B). In order to test whether the more distal cortical inputs are modulated by
356 NaP, we used the Thy1-ChR2 mice (Aceves Buendia et al., 2019; Arenkiel et al., 2007) that
357 expresses ChR2 in corticostriatal fibers (Figure 5C), but neither in the PfN (Figure 5–figure
358 supplement 1B) nor in the pedunculopontine nucleus (Gradinaru et al., 2009) that also
359 provides monosynaptic glutamatergic projection to CINs (Assous et al., 2019). The
360 monosynaptic EPSPs (Figure 5–figure supplement 1A) elicited by cortical inputs to CINs in
361 these mice were unaffected by ranolazine ($n = 11$ neurons, $N = 6$ mice, $P = 0.74$, Wilcoxon
362 signed-rank test, Figure 5D). Moreover, ranolazine had no effect on paired-pulse ratios
363 (Aceves Buendia et al., 2019) at either synapse (Figure 5–figure supplement 1C), ruling out a
364 presynaptic mechanism-of-action. Thus, we conclude that the post-synaptic modulation of
365 glutamatergic inputs to CINs by NaP currents corresponds to the spatial distribution of these
366 currents as derived from the quasi-linear properties of CINs and from our 2PLSM imaging of
367 bAPs.

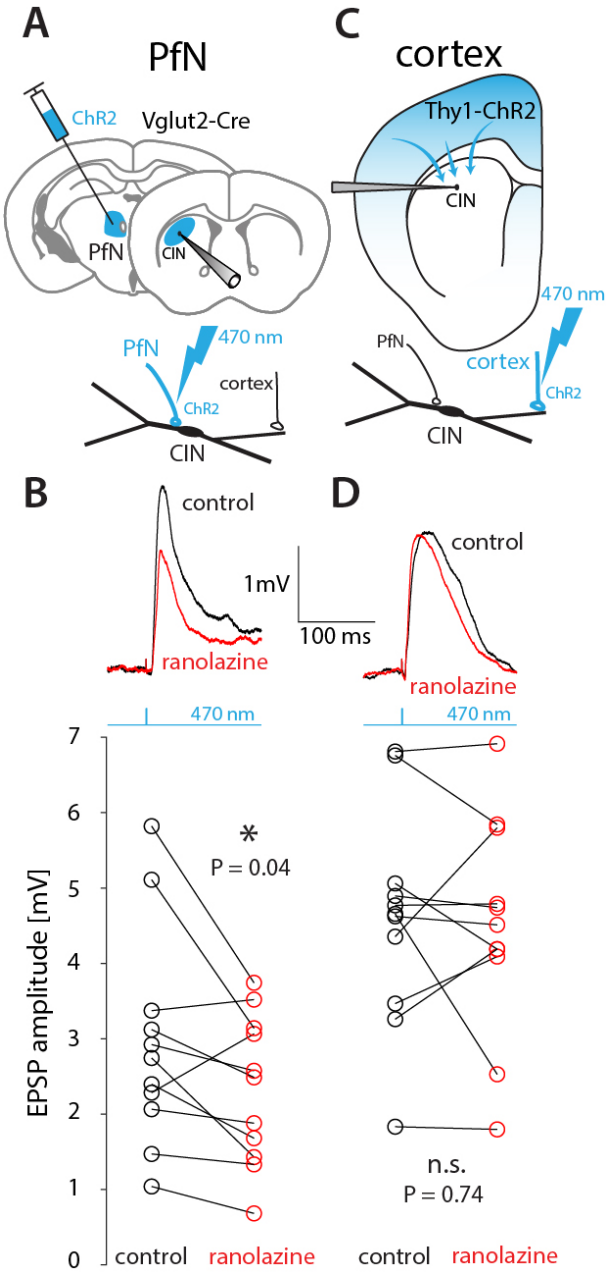

Figure 5: Thalamic – but not cortical EPSPs – onto CINs are boosted by NaP currents in healthy mice. A. The parafascicular nucleus (PfN) of Vglut2-Cre mice was inoculated with AAVs harboring Cre-dependent ChR2, so that 470 nm LED illumination of striatal slices activated monosynaptic PfN terminals while CINs were patched in current clamp mode. **B.** Optogenetically evoked thalamic EPSPs in CINs (held between –50 mV and –60 mV) were reduced by 30 µM ranolazine. **C.** CINs were patched in current clamp in Thy1-ChR2 mice, so that 470 nm LED illumination of striatal slices activated nominally cortical terminals. **D.** Optogenetically evoked monosynaptic cortical EPSPs were unaffected by ranolazine.

368

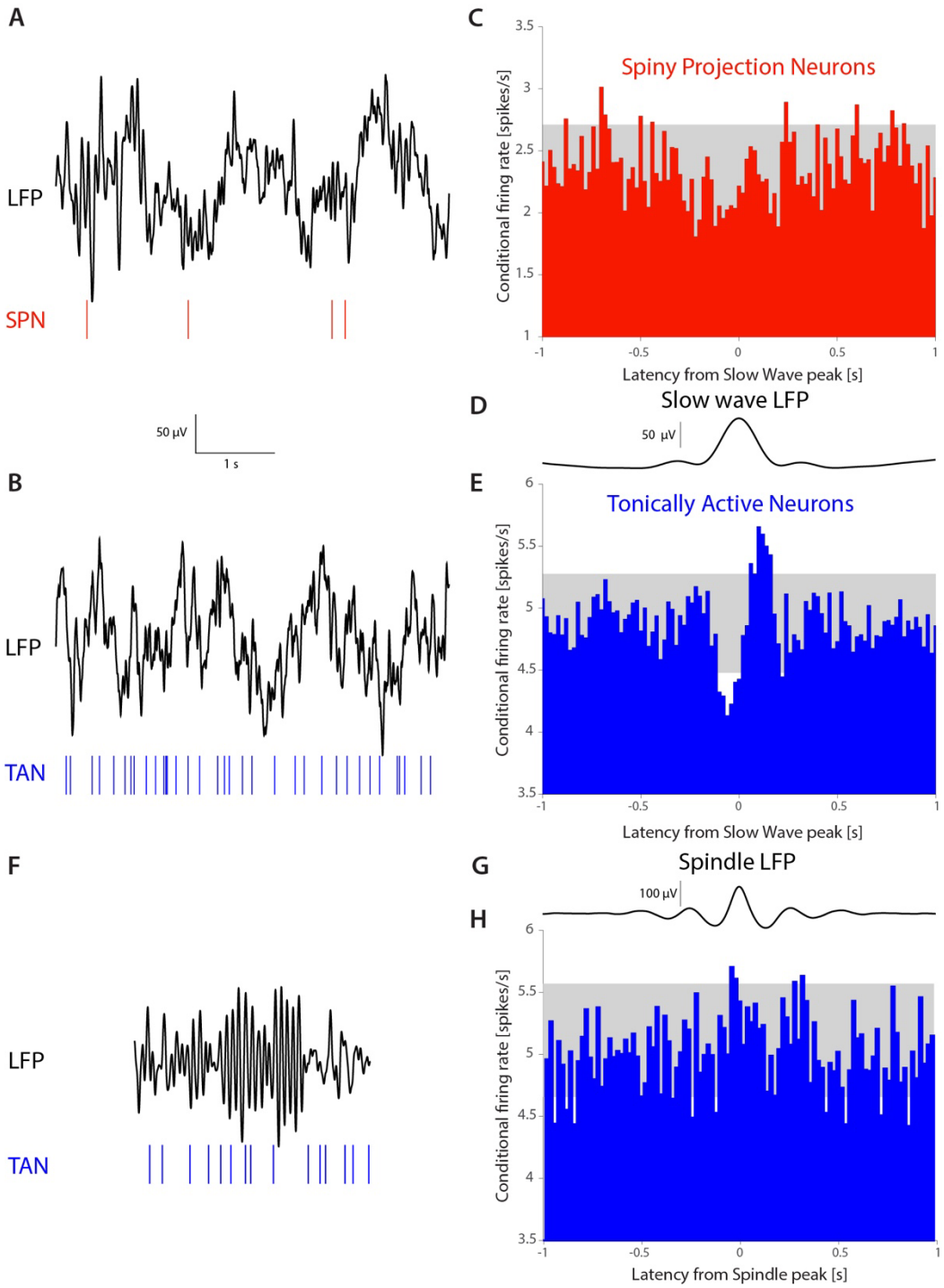

Figure 6: TANs, but not SPNs, exhibit a pause-like response to slow-wave events occurring during natural non-REM sleep in non-human primates (NHPs). A. simultaneous recording of LFP and an SPN in an NHP during N2 and N3 stages of sleep. **B.** simultaneous recording of LFP and a TAN in an NHP during N2 and N3 stages of sleep. **C.** SPN firing rate conditioned on the occurrence of an LFP slow wave event (6,065 triggers). **D.** Average striatal LFP signal triggered on the occurrence of slow wave events (see Materials and Methods). **E.** TAN firing rate conditioned on the occurrence of slow wave event (28,603 triggers). **F**. simultaneous recording of LFP and a TAN in an NHP during a sleep spindle. **G.** Average striatal LFP signal triggered on the occurrence of a sleep spindle (see Materials and Methods). **H.** TAN firing rate conditioned on the occurrence of a sleep spindle (5,829 triggers). Gray box indicates the 99% confidence intervals.

369 Tonically active neurons in non-human primates exhibit a pause-like response to slow wave
370 oscillations during sleep

371 Our data, alongside previous studies (Beatty et al., 2015), demonstrate that
372 somatodendritic HCN currents give rise to resonances in the subhertz range in CIN surface
373 membranes. In contrast, SPNs exhibit no resonance (Beatty et al., 2015). This suggests CINs
374 in intact animals may exhibit increased sensitivity to oscillatory inputs in that frequency
375 range, whereas SPNs should not. Delta waves in the electroencephalogram (EEG) and in
376 cortical and sub-cortical local field potentials (LFP) are prominent during non-REM sleep
377 across species (Brown et al., 2012; Liu and Dan, 2019), including in non-human primates
378 (NHPs) (Mizrahi-Kliger et al., 2018). Because the LFP is widely thought to represent
379 subthreshold cellular activity, affected by afferent and recurrent synaptic inputs (Buzsáki et
380 al., 2012), we hypothesized that the tonically active neurons (TANs) in the NHP striatum –
381 that are comprised primarily of CINs (Aosaki et al., 1995; Kawaguchi, 1993; Wilson et al.,
382 1990) – will exhibit stronger entrainment to slow-wave LFP events during sleep, while SPNs
383 under the same conditions will not. Indeed, triggering the spike trains of TANs and SPNs
384 (from $N = 2$ NHPs) on slow wave events that occur during sleep stages N2 and N3 (Mizrahi-
385 Kliger et al., 2018; Riedner et al., 2007), which represent relatively deep non-REM sleep,
386 demonstrates that while the firing rate of SPNs was unaffected ($n = 83$), the firing rates of
387 TANs ($n = 122$) was modulated by these slow-wave events (Figure 6A-E). In contrast, the
388 TANs firing was not modulated during higher frequency sleep spindle events (Figure 6F-H),
389 in agreement with the subhertz membrane resonance peak we observed in the acute slice
390 experiments. Importantly, the biphasic response exhibited by TANs to slow-wave events
391 bears a striking resemblance to the "classical" TAN response to external cues (Aosaki et al.,
392 1995; Apicella et al., 1991; Joshua et al., 2008; Kimura et al., 1984). Because these responses
393 in awake primates require an intact thalamic projection (Bradfield et al., 2013; Goldberg and
394 Reynolds, 2011; Matsumoto et al., 2001; Schulz and Reynolds, 2013; Smith et al., 2004;
395 Yamanaka et al., 2018) (and there is no reason to assume that this is altered in sleep), our
396 findings (Figure 6) provide support to the hypothesis that the CIN membrane resonance
397 contributes to a thalamically-driven biphasic CIN response during slow-wave sleep, possibly
398 because this projection terminates proximally on CINs. Importantly, because the primates are
399 asleep in a sound-proof room, this is, to the best of our knowledge, the first report of striatal
400 TANs responding to an internally-generated brain event, and not an external saliency-related
401 cue.

402 **Discussion**

403 Quasi-linear dendritic properties of CINs and the non-uniform distribution of their active
404 conductances

405 In the current study, we applied a cable-theoretic and optogenetics-based formalism –
406 that we developed previously to study dendritic properties of SNr neurons (Tiroshi and
407 Goldberg, 2019) – to study the dendritic properties of CINs. Unlike SNr neurons that were
408 found to act like passive linear cables exhibiting no voltage dependent properties, we find
409 that CIN dendrites exhibit both amplification and resonances in a voltage dependent manner:
410 amplification is more prominent at depolarized subthreshold potentials (approximately –55
411 mV), whereas resonances are more prominent at more hyperpolarized potentials
412 (approximately –70 mV). Moreover, we found that our method is able to provide information
413 about where in the dendritic arbor these quasi-linear properties are localized. We extracted
414 boosting (μ_n) and resonance (μ_h) parameters for proximal vs. full-field illumination, and
415 found that the magnitude of both parameters is smaller when the entire dendritic arbor is
416 illuminated. In other words, activating more of the distal dendritic membrane dilutes the
417 amplifying and resonating effects, meaning that the additional membrane illuminated in the
418 full-field condition contributed less to amplification and resonances. The simplest
419 interpretation of this finding is that the active conductances that give rise to amplification and
420 resonance are more highly expressed proximally and apparently taper off farther out in the
421 dendritic arbor. We identified the relevant currents by studying the quasi-linear properties of
422 CIN somata with voltage perturbations. We found that amplification is TTX-sensitive and
423 therefore arises from Nav channels, that give rise to the NaP current. Similarly, we found that
424 resonances require HCN channels.

425 We used one-direct and two indirect methods to validate the preferentially proximal
426 localization of NaP currents. First, TTX application revealed that boosting occurs only at the
427 soma (Figure 2B) and in proximal (but not distal, Figure 3F) dendritic membranes.
428 Importantly, the TTX results demonstrate that our conclusion that boosting is restricted to the
429 soma and proximal dendrites is *independent* of the quasi-linear model fit. Second, we
430 implemented a widely-used approach of estimating the distance of dendritic invasion of bAPs
431 by imaging the Ca^{2+} influx that accompanies them (Carter and Sabatini, 2004; Day et al.,
432 2008; Goldberg et al., 2009; Kerr, 2004; Rehani et al., 2019; Tanimura et al., 2016). We
433 found – not unlike in SPN neurons – that bAPs maintain their amplitude out to 70 μm from

434 the soma and then begin to decay, suggesting that Nav currents that support bAP propagation
435 taper off from that point onwards. Because strictly speaking a change in Ca^{2+} transients could
436 result from a change in the concentration of voltage-activated Ca^{2+} channels, future work can
437 verify our results by directly testing where locally puffed TTX attenuates the bAP (perhaps
438 even with the use of voltage sensitive probes). Second, we demonstrated that only thalamic –
439 but not cortical – EPSPs exhibit sensitivity to the selective NaP blocker. Because the thalamic
440 terminals are located more proximally (Lapper and Bolam, 1992; Mamaligas et al., 2019;
441 Thomas et al., 2000), this provides further evidence that NaP currents are more prominent
442 locally. The preferential localization of HCN currents proximally in CIN dendrites requires
443 additional validation, particularly because other neurons exhibit an opposite pattern (Berger
444 et al., 2001; Harnett et al., 2015; Kole et al., 2006). However, we were less interested in
445 validating the proximal localization of HCN currents, because unlike NaP currents, activation
446 of HCNs is conditioned on CINs being actively (after-)hyperpolarized, during which bAPs
447 are unlikely to occur. We did however test a context in which HCN currents, and the
448 resonance they underlie, are likely to affect CIN collective dynamics. We found that TANs
449 respond biphasically to internally-generated slow wave activity during sleep, but not to sleep
450 spindles. This preferential entrainment is consistent with the fact that CIN membranes exhibit
451 a resonance in the subhertz range as found by us and others (Beatty et al., 2015). The
452 elevated impedance (or frequency-dependent access resistance) in this range means that
453 inputs fluctuating in this range will more efficiently depolarize the CINs, and therefore more
454 likely to trigger additional action potentials than inputs fluctuating at a frequency that is far
455 from the resonance frequency. Accordingly, SPNs that do not exhibit resonances (Beatty et
456 al., 2015) are not entrained by the slow wave oscillation. Our findings in sleeping NHPs are
457 at odds with various rodent studies that found that cortical slow-wave activity is weakly
458 associated with the discharge of TANs in anesthetized rodents, and more strongly associated
459 with SPN activity (Goldberg et al., 2003; Mahon, 2001; Reig and Silberberg, 2014; Schulz et
460 al., 2011; Sharott et al., 2012; Stern et al., 1998). These differences may be attributable to
461 species differences and/or differences between natural sleep and anesthesia, which may differ
462 in the degree to which thalamic *vs.* cortical inputs engage striatal neurons. Moreover, the
463 dendritic nonlinearities in SPNs (Plotkin et al., 2011) may be preferentially engaged during
464 anesthesia, thereby causing SPNs to respond more strongly under anesthesia than during
465 natural sleep.

466 Advantages and limitations of the quasi-linear formalism and the optogenetics-based
467 approach

468 As mentioned in the Introduction, the quasi-linear approach provides a tool to
469 characterize membrane excitability in general functional terms, without requiring the
470 complete biophysical characterization of membrane currents. Unfortunately, the method is
471 not invertible: even after estimating all the quasi-linear parameters one cannot deduce the full
472 biophysical characterization of the underlying channels even if one has a precise
473 mathematical model of these channels. Moreover, even though we extracted the values of μ_n
474 and μ_h, we do not know how to translate them into a quantitative measure of channel density.
475 Still, the ability to compare parameters for various spatial illumination patterns enables us to
476 reach qualitative conclusions regarding relative channel density. Additionally, our attribution
477 of μ_n to NaP and μ_h to HCN is only provisional. CINs possess other channels that have a
478 major influence on their firing patterns such as A-type, inward rectifying, and various Ca^{2+}-
479 activated K^+ channels, to mention a few (Bennett et al., 2000; Deng et al., 2007; Goldberg et
480 al., 2009; Goldberg and Wilson, 2010, 2005; McGuirt et al., 2021; Oswald et al., 2009; Song
481 and Surmeier, 1996; Wilson, 2005; Wilson and Goldberg, 2006), that were not included in
482 our analysis. Future work should elaborate how these and other channels contribute to the
483 quasi-linear properties of CINs and their dendrites.
484 Using optogenetics provides another level of practicality. The seminal studies that
485 characterized the filtering properties of dendrites or pyramidal neurons (Berger et al., 2001;
486 Goldberg et al., 2007; Hutcheon et al., 1996; Ulrich, 2002) required dual soma-dendrite
487 patching which is not practical for all neuronal types whose dendrites taper off rapidly.
488 Expressing opsins in the membrane being activated, as we did, means that a single somatic
489 patch electrode can suffice to conduct the quasi-linear characterization. We currently use this
490 approach to illuminate large regions of the dendritic arbor simultaneously, which means we
491 can only derive large-scale dendritic properties. In the future, localized laser stimulation of
492 dendritic regions (visualized with the help of a fluorescent marker in the patch pipette), or
493 even two-photon laser activation of opsins (provided one can find stimulation parameters that
494 do not harm the dendrites) could be used as an alternative approach. On the backdrop of
495 optogenetics being utilized almost exclusively to study circuit mapping (Häusser, 2021; Kim
496 et al., 2017; Petreanu et al., 2009) by expressing opsins presynaptically, we believe our study
497 joins other studies (Higgs and Wilson, 2017; Tiroshi and Goldberg, 2019) to underscore the

498 value of using opsins expressed postsynaptically to study neuronal – even dendritic –
499 excitability.

500 Somatic amplification and resonance in CINs

501 We preceded our optogenetic characterization of dendritic nonlinearities with the
502 electrical characterization of quasi-linear somatic properties using a sinusoidal voltage
503 command applied through the patch pipette. As previously reported by Beatty and
504 collaborators (Beatty et al., 2015), CIN somata exhibit a membrane resonance in the subhertz
505 range, that depends on the holding potential. However, while Beatty and collaborators found
506 that an amplified resonance is present in the more depolarized (approximately – 55 mV)
507 range, we found that the resonance is only pronounced in the more hyperpolarized
508 (approximately –70 mV) range, where it depends on the HCN current. It is possible that the
509 resonances observed by Beatty and collaborators (Beatty et al., 2015) at –55 mV arose from
510 ineffective clamping of dendrites with the slightly higher resistance electrodes used in that
511 study. In support of this proposition, we also found evidence for the resonance arising from
512 unclamped (dendritic) membranes. When the CINs were clamped at –55 mV, while somatic
513 voltage perturbations did not produce a resonance, optogenetic stimulation (both proximal
514 and full field) at 0.4 Hz produced a more negative phase than at the neighboring 0.2 Hz and
515 0.6 Hz stimulation (Figure 3C, green arrow). This downward deflection in phase is
516 reminiscent of the fullblown negative subhertz region that occurred with optogenetic
517 stimulation when the CINs were clamped at –70 mV (Figure 3D). Thus, it is likely that
518 resonance originated in both studies from dendritic HCN currents. Because in the study of
519 Beatty and collaborators (Beatty et al., 2015) TTX lowered the impedance, without removing
520 the subhertz resonance peak, we conclude that the effect of TTX in both studies is to remove
521 the NaP-dependent boosting, without directly affecting resonance. It also seems that the
522 location of the peak amplitudes estimated by Beatty and collaborators (Beatty et al., 2015) is
523 perhaps 1 Hz larger than the location of the peaks in our study. However, this difference
524 could result from the fact that they used a chirp stimulation where the frequency increases
525 continuously, whereas we used several periods of perfect sinusoidal waveforms with a
526 discrete set of frequencies. Moreover, it can be shown mathematically that for the quasi-
527 linear model the zero crossing in the phase response occurs at a slightly smaller frequency
528 than the peak in the amplitude response, so this may also contribute to the impression that the

529 resonance frequency observed in our experiments is slightly different from that observed in
530 Beatty and collaborators (Beatty et al., 2015).

531 Dendritic contribution to capacity of CINs to differentiate between their excitatory inputs

532 In NHPs, TANs that are comprised primarily of CINs (Aosaki et al., 1995; Goldberg
533 and Wilson, 2010; Kawaguchi, 1993; Wilson et al., 1990), encode – through a brief pause in
534 their tonic firing – external stimuli that are salient (and often unexpected, even conveying a
535 stop or behavioral shift signal (Aoki et al., 2018; Thorn and Graybiel, 2010)) or stimuli that
536 are associated with reward (Apicella et al., 1991; Goldberg and Reynolds, 2011; Kimura et
537 al., 1984). The pause response requires an intact projection from the PfN of the thalamus
538 (Bradfield et al., 2013; Goldberg and Reynolds, 2011; Matsumoto et al., 2001; Schulz et al.,
539 2011; Schulz and Reynolds, 2013; Smith et al., 2004; Yamanaka et al., 2018), indicating that
540 TANs are attuned to thalamic input. While TANs do not respond to ongoing movement
541 (Aosaki et al., 1994; Apicella et al., 1991; Kimura et al., 1984; Raz et al., 1996), and hence
542 seem less attuned to sensorimotor cortical input (Sharott et al., 2012), CIN activity in awake
543 behaving mice is strongly modulated by self-initiated movements (Gritton et al., 2019; Howe
544 et al., 2019; Yarom and Cohen, 2011). Nevertheless, slice physiology studies in rodents
545 (Aceves Buendia et al., 2019; Assous, 2021; Assous et al., 2017; Ding et al., 2010; Johansson
546 and Silberberg, 2020; Kosillo et al., 2016; Threlfell et al., 2012) clearly show that thalamic
547 inputs to CINs are stronger in the sense that they give rise to larger EPSPs (Johansson and
548 Silberberg, 2020) and can trigger a pause-like responses (Ding et al., 2010), whereas cortical
549 inputs to most CINs (Mamaligas et al., 2019) are weaker in that they give rise, in acute slices,
550 to smaller EPSPs and cannot trigger the pause-like response – although this distinction is less
551 pronounced in anesthetized rodents (Doig et al., 2014). Thus, it is clear that CINs
552 differentiate between these two excitatory inputs and respond differently to them. A major
553 contributor to the CINs' capacity to dissociate thalamic and cortical input is the differential
554 distribution of their respective terminals on the dendritic arbor: thalamic input terminate
555 perisomatically and on proximal dendrites, whereas cortical input terminates on distal
556 dendrites (Doig et al., 2014; Lapper and Bolam, 1992; Mamaligas et al., 2019; Thomas et al.,
557 2000). Our finding that the higher expression of NaP currents in proximal dendrites
558 preferentially boosts thalamic over cortical inputs, suggests that active conductances are
559 expressed in CIN dendrites in a manner that corresponds and reinforces the effect of the
560 spatial separation between the terminals of the two inputs.

561 Adaptive changes in dendritic excitability in movement disorders

562 The capacity of the CIN dendritic excitability to mirror the distribution of afferent
563 terminals is also an adaptive process. We previously reported that CIN dendritic excitability
564 is elevated in the Q175 mouse model of Huntington's disease (HD) (Tanimura et al., 2016).
565 In contrast to control (Thy1-ChR2) mice in which cortical EPSPs in CINs are insensitive to
566 ranolazine (Figure 5), cortical excitatory postsynaptic currents (EPSCs) in CINs from Q175
567 mice (crossed with Thy1-ChR2 mice) are strongly reduced by ranolazine. The acquired
568 dependence of distal cortical inputs on NaP currents in Q175 mice results from an
569 upregulation of the NaP current, which was also evidenced by bAPs invading farther out into
570 the CINs' dendritic arbor (Tanimura et al., 2016). This elevated excitability in the Q175
571 mouse is probably a homeostatic response aimed at elevating the postsynaptic sensitivity to
572 the remaining synaptic contents after the loss of afferent cortical and thalamic inputs
573 observed in HD mouse models (Deng et al., 2013). Because thalamostriatal inputs are also
574 altered in models of Parkinson's disease (PD) (Aceves Buendia et al., 2019; Parker et al.,
575 2016; Tanimura et al., 2019), future work should determine whether the excitability of CIN
576 dendrites is altered in these models, as well. Importantly, dendrites are positioned at the
577 interface between synaptic inputs and the intrinsic properties of CIN. While changes in
578 synaptic transmission and intrinsic excitability of CINs have received attention in models of
579 PD, HD and other movement disorders (Abudukeyoumu et al., 2019; Aceves Buendia et al.,
580 2019; Choi et al., 2020; Ding et al., 2006, 2011; Eskow Jaunarajs et al., 2015; Mallet et al.,
581 2019; Paz et al., 2021; Pisani et al., 2007; Plotkin and Goldberg, 2019; Poppi et al., 2021;
582 Tanimura et al., 2019; Tubert and Murer, 2021), studying alterations in dendritic excitability
583 in these models is a complementary approach that remains largely unchartered territory.
584 The membrane channels that are expressed in CINs (e.g., Nav, HCN, Kv4, etc.) are
585 targets for neuromodulation under normal, healthy circumstances (Deng et al., 2007; Helseth
586 et al., 2021; Maurice, 2004; Song and Surmeier, 1996). Therefore, it is likely that the
587 dendritic excitability of CINs can be modulated under physiological conditions, as well, as a
588 way to adjust the tuning of CINs to their afferent inputs. Conversely, if boosting and
589 resonances are present primarily proximally, the selective tuning of CINs to subhertz slow-
590 wave oscillations is probably stronger for thalamic inputs (that terminate proximally) than for
591 cortical inputs. Future experiments can address this issue by testing how silencing the PfN
592 affects the observed entrainment of TANs to slow-waves (Figure 6).

In summary, we have used a new optogenetics-based approach, complemented by other electrophysiological and imaging approaches, to demonstrate that the spatial localization of active dendritic conductances that endow CIN dendrites with quasi-linear filtering properties corresponds to the spatial distribution of their two main afferent excitatory inputs. This matching up of presynaptic terminals with post-synaptic excitability, probably contributes to the capacity of CINs to respond differentially to cortical and thalamic inputs. Sensorimotor information of cortical origin seems to be integrated continuously in a moment-by-moment fashion. In contrast, thalamic inputs lead to abrupt pauses in TAN firing, even in response to internally-generated brain-states (e.g., during slow-wave activity). The possibility that dendritic arbors adapt to the spatiotemporal patterns of afferent inputs is likely an important principle of neural computation that deserves further attention, particularly in the framework of autonomously active neurons such at CINs, SNr neurons and other basal ganglia pacemakers.

Materials and Methods

Key Resources Table				
Reagent type (species) or resource	**Designation**	**Source or reference**	**Identifiers**	**Additional information**
Genetic reagent (M. musculus)	B6;129S6-Chattm2(cre)Lowl/J	The Jackson Laboratory	Strain #:006410 RRID:IMSR_JAX:006410	ChAt-ires-CRE
Genetic reagent (M. musculus)	B6;129S-Gt(ROSA)26Sortm32(CAG-COP4*H134R/EYFP)Hze/J	The Jackson Laboratory	Strain #:012569 RRID:IMSR_JAX:012569	Ai32-conditional ChR2
Genetic reagent (M. musculus)	STOCK Slc17a6tm2(cre)Lowl/J	The Jackson Laboratory	Strain #:016963 RRID:IMSR_JAX:016963	Vglut2-ires-cre
Chemical compound, drug	Mecamylamine hydrochloride	Sigma-Aldrich	Lot # 019M4108V CAS: 826-39-1	

Chemical compound, drug	Atropine sulfate salt monohydrate	Sigma-Aldrich	Lot # BCBH8339V CAS No.: 5908-99-6	
Chemical compound, drug	SR 95531 hydrobromide (Gabazine)	Hello Bio	CAS: 104104-50-9	
Chemical compound, drug	DNQX	TOCRIS	CAS: 2379-57-9	
Chemical compound, drug	D-AP5	Hello Bio	CAS:79055-68-8	
Chemical compound, drug	CGP 55845 hydrochloride	Hello Bio	CAS: 149184-22-5	
Chemical compound, drug	Dihydro-β-erythroidine hydrobromide	TOCRIS	CAS: 29734-68-7	
Chemical compound, drug	Ranolazine dihydrochloride	Sigma-Aldrich	CAS Number: 95635-56-6	Product Number R6152
Chemical compound, drug	ZD7288	MedChemExpress	CAS No. : 133059-99-1	Synonyms: ICI D7288
Chemical compound, drug	Tetrodotoxin citrate	Hello Bio	CAS: 18660-81-6	
Chemical compound, drug	4-Aminopyridine	Sigma-Aldrich	CAS Number: 504-24-5	
Chemical compound, drug	Phosphate buffered saline tablets	Sigma-Aldrich	MDL number: MFCD00131855	Product Number P4417
Chemical compound, drug	Paraformaldehyde	Sigma-Aldrich	CAS Number: 30525-89-4	

Chemical compound, drug	XYLAZINE AS HYDROCHLORIDE	EUROVET ANIMAL HEALTH B.V	CAS: 082-91-92341-00	
Chemical compound, drug	CLORKETAM	VETOQUINOL	CAS: 1867-66-9	
Chemical compound, drug	Meloxicam	Chanelle Pharmaceuticals Manufacturing ltd	CAS Number: 71125-38-7	
Chemical compound, drug	isoflurane	Primal Critical Care	CAS Number: 26675-46-7	
Software	MATLAB	MathWorks	RRID:SCR_001622	Data analysis
Software	XPPAUT	X-Windows Phase Plane plus Auto	RRID:SCR_001996	Modelling
Software	WinWCP	University of Strathclyde Glasgow	RRID:SCR_014713	Data acquisition
Software	FEMTOSmart Software: MESc	FEMTONICS	RRID:SCR_018309	2P Data acquisition
Software	NIS-Elements Basic Research	Nikon instruments	RRID:SCR_002776	Confocal images acquisition
Software	Signal 6	Cambridge Electronic Design	RRID:SCR_017081	
Software	AlphaLab SnR	Alpha-Omega Engineering	https://www.alphaomega-eng.com/	
Software	Electrode Positioning System	Alpha-Omega Engineering	https://www.alphaomega-eng.com/	

Others	Model 940 Small Animal Stereotaxic Instrument with Digital Display Console	Kopf Instruments	https://kopfinstruments.com/product/model-940-small-animal-stereotaxic-instrument-with-digital-display-console/	
Others	Sound-attenuating room	IAC acoustics	https://www.iacacoustics.com/	
Others	Glass-coated Tungsten electrodes	Alpha-Omega Engineering	https://www.alphaomega-eng.com/	
Others	Pre-gelled surface electrodes	Rhythmlink International	https://rhythmlink.com/	
Others	subdermal needle electrodes	Rhythmlink International	https://rhythmlink.com/	
Others	Infra-red camera	Norpix Inc., Canada	https://www.norpix.com/	

608 Ethics statement: All experimental protocols were conducted in accordance with the National
609 Institutes of Health Guide for the Care and Use of Laboratory Animals, and with the Hebrew
610 University guidelines for the use and care of laboratory animals in research. The experiments
611 adhered to, received prior written approval from and were supervised by the Institutional
612 Animal Care and Use Committee of the Faculty of Medicine, under protocols: MD-16-13518-
613 4 (H.B.) and MD-18-15657-3 (J.A.G.).

614 Mice: Homozygous Ai32 (RCL-ChR2(H134R)/EYFP) mice (The Jackson laboratory [Jax]
615 stock: 012569) that express floxed ChR2 and an EYFP fusion protein under the CAG
616 promoter were crossed with homozygous ChAT-IRES-Cre (Δneo) mice the express Cre
617 recombinase under the choline acetyltransferase promoter (Jax stock: 031661). The ChAT-
618 ChR2 offspring (4-8 weeks old/both sexes) were used for the majority of experiments. To
619 investigate corticostriatal transmission, we used homozygous transgenic Thy1-ChR2 mice
620 (B6.Cg-Tg (Thy1-COP4/EYFP) 18Gfng/1, Jax stock: 007612), that express ChR2 under the
621 Thy1 promoter in cortical neurons (Arenkiel et al., 2007). To investigate thalamostriatal
622 transmission, we used Vglut2-ires-Cre mice (Jax stock: 016963).

623 Non-Human Primates (NHPs): Data were obtained from two healthy, young adult, female
624 vervet monkeys. The monkeys were habituated to sleeping in a primate chair, positioned in a
625 dark, double-walled sound-attenuating room. The primate chair restrained the monkeys' hand

626 and body movements but otherwise allowed them to be in a position similar to their natural
627 (sitting) sleeping posture. Detailed sleep habituation, surgery and sleep staging were reported
628 previously (Mizrahi-Kliger et al., 2018). For extracellular recordings, the monkeys' heads
629 were immobilized with a head holder and eight glass-coated tungsten microelectrodes were
630 advanced the dorsal striatum. Electrical signals were amplified with a gain of 20, filtered
631 using a 0.075 Hz (2 pole) to 10 kHz (3 pole) Butterworth filter and sampled at 44 kHz by a
632 16-bit analog/digital converter. Spiking activity was sorted online using a template matching
633 algorithm. The striatum was identified based on its stereotaxic coordinates according to MRI
634 imaging and primate atlas data (Martin and Bowden, 2000). Tonically active neurons (TANs)
635 and spiny projection neurons (SPNs) were identified using real-time assessment of their
636 electrophysiological features. Spiking and local field potentials (LFP) were recorded only for
637 identified recording sites with stable recording quality (i.e., where single-neuron spiking
638 yielded an average isolation score ≥0.85).
639 We followed established procedures for slow wave detection in the LFP (Riedner et al.,
640 2007). Briefly, the LFP signal was filtered at the 0.5-4 Hz range and putative slow wave events
641 whose duration was 0.25-2 seconds were kept for further analysis. Next, the slow wave peaks
642 were sorted according to their amplitude. Artifacts were removed by discarding all events
643 whose amplitude exceeded 5 standard deviations above the mean. Finally, conditional firing
644 rate analysis was only performed on 30% of the slow wave events with the highest amplitude.
645 Conventional procedures were also used for sleep spindle detection in the LFP (Sela et al., 2016,
646 p. 2016). Briefly, the detection algorithm was only used for striatal sites whose LFP showed
647 significant 10-17 Hz (spindle range) activity. LFP was filtered at the 10-17 Hz range and the
648 Hilbert transform was then used to extract the instantaneous amplitude. Events exceeding 3
649 standard deviations above the mean were deemed potential spindle events, and a threshold of
650 one half of a standard deviation above the mean was used to detect the start and end point of an
651 individual sleep spindle. A potential sleep spindle was defined as such only if it lasted 0.5-3
652 seconds, and provided it did not exhibit a relatively high (more than 4.5 standard deviations
653 above the mean) amplitude in a control 20-30 Hz range. The spindle data were obtained using
654 a 4-pole 4-25 Hz Butterworth filter.

655 Histology: An 8 weeks old male Thy1-ChR2 mouse was deeply anesthetized with a terminal
656 dose of ketamine-xylazine followed by perfusion through the heart of cold PBS and 4% PFA.
657 The removed brain was kept overnight at 4˚C in 4% PFA. The next day, the brain was
658 washed 3 X 15 minutes before 50 µm coronal slices of the PfN were cut with a vibratome

659 (Leica VT1000S). VECTASHIELD (Vector Laboratories) was applied onto mounted slices
660 to protect from bleaching. Coronal slices of the PfN were imaged using confocal microscope
661 (Nikon A1R) using 10x lens and a 20x oil immersion lens to visualize constitutive EYFP
662 expression.

663 Stereotaxic viral inoculation in Vglut2-ires-Cre mice: Mice were deeply anesthetized with
664 isoflurane in a non-rebreathing system (2.5% induction, 1-1.5% maintenance) and placed in a
665 stereotaxic frame (Kopf Instruments, Tujunga, CA). Temperature was maintained at 35˚C
666 with a heating pad, artificial tears were applied to prevent corneal drying, and animals were
667 hydrated with a bolus of injectable saline (10 ml/kg) mixed with analgesic (2.5 mg/kg
668 Meloxicam). Stereotaxic injections into caudal intralaminar nuclei of thalamus were
669 performed under aseptic conditions. Adeno-associated viruses (AAV) serotype 9 carrying
670 double-floxed fusion genes for hChR2 (E123A) and EYFP under an EF1a promoter
671 (University of Pennsylvania Vector Core, Addgene #35507) were used to transfect PfN
672 neurons. Injection coordinates were from Bregma: lateral, 0.65 mm; posterior, 2.3 mm; and
673 3.35 mm depth from surface of brain (Rehani et al., 2019). A small hole was bored into the
674 skull with a micro drill bit and a glass pipette was slowly inserted at the PfN coordinates. To
675 minimize backflow, solution was slowly injected; a total volume of 250 nl (>2.5x1012
676 GC/ml) of the AAV constructs was injected over a period of approximately 1.5 min and the
677 pipette was left in place for 5 min before slowly retracting it. Slice physiology experiments
678 were conducted 2-3 weeks after surgery.

679 Slice preparation: Mice were deeply anesthetized with ketamine (200 mg/kg)–xylazine (23.32
680 mg/kg) and perfused transcardially with ice-cold-modified artificial cerebrospinal fluid
681 (ACSF) bubbled with 95% O_2–5% CO_2, and containing (in mM) 2.5 KCl, 26 $NaHCO_3$, 1.25
682 Na2HPO4, 0.5 $CaCl_2$, 10 $MgSO_4$, 0.4 ascorbic acid, 10 glucose and 210 sucrose. The brain
683 was removed, and 275 µm thick sagittal slices containing the striatum were cut in ice-cold-
684 modified ACSF. Slices were then submerged in ACSF, bubbled with 95% O_2–5% CO_2,
685 containing (in mM) 2.5 KCl, 126 NaCl, 26 $NaHCO_3$, 1.25 Na_2HPO_4, 2 $CaCl_2$, 2 $MgSO_4$ and
686 10 glucose, and stored at room temperature for at least 1 h prior to recording.

687 Electrophysiological recording: The slices were transferred to the recording chamber
688 mounted on a Zeiss Axioskop 60X, 0.9 NA fixed-stage microscope and perfused with
689 oxygenated ACSF at 31ºC. During the optogenetic stimulation experiments, in order to
690 guarantee that the effects we measured were generated post-synaptically, the ACSF solution

691 contained (in μM) 10 DNQX to block AMPA receptors, 50 D-APV to block NMDA
692 receptors, 10 gabazine (SR95531) to block $GABA_A$ receptors, - 2 CGP55845 to block
693 $GABA_B$ receptors, 10 atropine to block muscarinic ACh receptors, and 10 mecamylamine to
694 block nicotinic ACh receptors. In the experiments in which optogenetics were used to
695 stimulate cortical or thalamic input we used the same blockers, except for DNQX which was
696 left out. An Olympus 40X, 0.8 NA water-immersion objective with a 26.5 mm field number
697 (FN) was used to examine the slice using standard infrared differential interference contrast
698 video microscopy. Patch pipette resistance was typically 4-5 MΩ when filled with recording
699 solutions. The junction potential estimated at 7-8 mV was not corrected. In EPSC
700 measurements, the intracellular solution contained (in mM): 127.5 $CsCH_3SO_3$, 7.5 CsCl, 10
701 HEPES, 10 TEA-Cl, 4 phosphocreatine disodium, 0.2 EGTA, 0.21 Na_2GTP, and 2 $Mg_{1.5}ATP$
702 (pH=7.3 with CsOH, 280-290 mOsm/kg). In the Ca^{2+} imaging experiments (see below) the
703 internal solution contained (in mM) 135 K-gluconate, 5 KCl, 2.5 NaCl, 5 Na-
704 phosphocreatine, 10 HEPES, 0.1 fluo-4 (Molecular Probes), 0.1 Alexa Fluor 568 (for
705 morphological visualization, Molecular Probes), 0.21 Na_2GTP, and 2 $Mg_{1.5}ATP$, pH 7.3 with
706 KOH (280–290 mOsm/kg). In all other experiments, the intracellular solution contained (in
707 mM) 135.5 KCH_3SO_3, 5 KCl, 2.5 NaCl, 5 Na-phosphocreatine, 10 HEPES, 0.2 EGTA, 0.21
708 Na_2GTP, and 2 $Mg_{1.5}ATP$, pH 7.3 with KOH (280–290 mOsm/kg). Electrophysiological
709 recordings were obtained with a MultiClamp 700B amplifier (Molecular Devices, Sunnyvale,
710 CA). Signals were filtered at 10 kHz online, digitized at 10 or 20 kHz and logged onto a
711 personal computer with the Signal 6 software (Cambridge Electronic Design, Cambridge,
712 UK). All reagents, drugs and toxins were purchased from either Merck/Sigma-Aldrich
713 (Darmstadt, Germany), Tocris Biosciences (Bristol, UK), MedChemExpress (Monmouth
714 Junction, NJ, USA) or HelloBio (Bristol, UK).

715 Voltage-perturbation experiments: CINs were held at either –55 mV or –70 mV and were
716 given an 83 second-long voltage command structured as a concatenated sequence of
717 sinusoids from a discrete set of frequencies ranging from 0.2 to 20 Hz with an amplitude of 2
718 mV (3 or 5 seconds per frequency, such that each frequency was represented by an integer
719 multiple of its fundamental period). Phase shifts between the voltage sinusoidal and the
720 somatic current response were determined by the location of the peak in the cross-correlation
721 function (CCF) of the two traces (whose units are mV·pA), for each stimulation frequency
722 and for each illumination condition. The impedance at each frequency, $|Z(f)|$, was calculated

723 from the maximal amplitude of the CCF as $|Z(f)| = (2\ \mathrm{mV})^2/\max(\mathrm{CCF})$ (so that its units are
724 GΩ).

725 Optogenetic stimulation: Optogenetic stimulation was performed with blue-light (470 nm)
726 LED illumination via the objective (Mightex, Toronto, ON, Canada). We used two spatial
727 illumination regimes: a) *proximal illumination* wherein an opaque disk with a central pinhole
728 was placed in the back focal plane of the 60X water-immersion objective such that a ~130
729 μm diameter region around the soma was illuminated (Tiroshi and Goldberg, 2019), thereby
730 targeting the soma and proximal dendrites; and b) *full-field illumination* of the entire slice
731 with a 5X air objective which excites the soma and the entire dendritic field. In all
732 experiments, LED light intensity was chosen such that stimulation generated comparable
733 current responses for both regimes. We used the same sequence of sinusoids described above,
734 only this time the voltage driving the LED was modulated (the minimal voltage was the
735 LED's voltage threshold, 40 mV). The phase delays were again calculated according to the
736 latency of the peak of the CCF between the LED voltage command and somatic current.
737 Note, that the phases were corrected by 0.5 (i.e., by π in radians) due to the fact that the ChR2
738 inward current is in antiphase with the LED's voltage command. The amplitude response was
739 calculated from the peak value of the CCF, normalized by the amplitude of the 470 nm LED
740 command (i.e., 1V for proximal illumination and 0.1 V for the full-field illumination, so that
741 its units are picoamperes).

742 To activate the excitatory synaptic inputs in the Thy1-ChR2 and in the Vglut2-mice a
743 full-field 470 nm LED 1 ms-long pulses were used with GABA, ACh and NMDA receptor
744 blockers in the ACSF. For EPSPs we average 25 trials (3 s intervals, and trials with spikes
745 were omitted). Paired pulse ratio (PPR) measurements consisted of 64 trials of two pulses
746 (100 ms apart, 3 s interval). The mean EPSC amplitude was calculated as the difference
747 between the mean peak current and the mean baseline current that preceded the pulse. PPR
748 was the ratio of the second mean EPSC to the first mean EPSC. To demonstrate that the
749 EPSCs were monosynaptic they were recorded before and after application of 1 μM TTX and
750 100 μM 4-AP (Petreanu et al., 2009).

751 To estimate the kinetics of the ChR2 currents, brief 1ms-long 470 nM LED pulses
752 (1V for proximal and 0.1 V for the full-field illumination) were repeated 250 times and the
753 resulting average current response was measured, and fit with an alpha function

$$A\left(e^{-t/\tau_r} - e^{-t/\tau_d}\right) \quad \text{(Eq. 1)}$$

754 to estimate the τ_r and τ_d, the rise and decay times, respectively.

755 Two-photon laser scanning microscopy (2PLSM): The two-photon excitation source was a
756 Chameleon Vision II tunable Ti:Sapphire pulsed laser (Coherent, Santa Clara, CA, USA)
757 tuned to 820 nm. The images were collected with the Femto2D system (Femtonics, Budapest,
758 Hungary) which includes two 3 mm galvo-scanners, one gated GaAsP and one multi-alkaline
759 non-descanned photomultiplier tube for imaging fluo-4 and Alexa Fluor, respectively. Z-
760 stacks of optical sections (spaced 2 µm apart) were collected using 0.2 µm pixels and 15 µs
761 dwell times. Optical and electrophysiological data were obtained using the software package
762 MES (Femtonics), which also integrates the control of all hardware units in the microscope.
763 The software automates and synchronizes the imaging signals and electrophysiological
764 protocols. Data was extracted from the MES package to personal computers using custom-
765 made code in MATLAB. We recorded spontaneously occurring bAPs with line scans at
766 various distances measured radially from the tip of the soma. Spike triggered averages of the
767 calcium measurements ($\Delta F/F_0$) were estimated and an alpha-function (Eq. 1) was fit to them.
768 The value of the peak of the fitted alpha-function was used as a measure of the size of the
769 spontaneous bAP at that location.

770 Drugs and Reagents: TTX was used to block voltage-activated Na^+ currents. Ranolazine was
771 used to block NaP. ZD7288 was used to block the HCN current. Gabazine (SR-95531) and
772 CGP 55845 were used to block $GABA_A$ and $GABA_B$ receptors, respectively. 4-
773 Aminopyridine (4-AP) was used to enable optogenetically-driven monosynaptic release in
774 the presence of TTX. All reagents, drugs and toxins were purchased from either
775 Merck/Sigma-Aldrich (Darmstadt, Germany), Tocris Biosciences (Bristol, UK) or HelloBio
776 (Bristol, UK).

777 Data analysis and statistics: Data were analyzed and curve fitting was performed using
778 custom code in Matlab (MathWorks, Natick, MA, USA). Simulations of the nonlinear
779 dendrite (Appendix 2) was were performed using XPPAUT (Ermentrout, 2002). The
780 nonparametric two-tailed Wilcoxon signed-rank test was used for matched samples and the
781 Wilcoxon rank-sum test was used for independent samples. The parametric ANCOVA test
782 was used to test significant changes in the amplitude and phase curves as a function of the

natural logarithm of the frequencies (an operation which spreads out this independent parameter more uniformly). Null hypotheses were rejected if the P-value was below 0.05.

For the TAN and SPN locking to slow wave or spindle peak analysis, confidence intervals (at P-value of 0.01) were calculated based on the distribution of conditional firing rates 1 s before and after the slow wave peak.

Parameter fitting to the phase delay: In our previous study (Tiroshi and Goldberg, 2019), we modeled the dendritic arbor as a semi-infinite cable with a homogeneous quasi-linear membrane (i.e., the current density of each nonlinearity is constant along the dendrite). When a segment of length *r* (measured in units of the dendrite's space constant) from the soma is activated with a sinusoidal current injection, the dendritic phase delay is given by

$$\phi_d = \frac{1}{2\pi}\left(\tan^{-1}\frac{q}{p} - \tan^{-1}\frac{\sin qr}{e^{pr} - \cos qr}\right) \qquad \text{(Eq. 2)}$$

where

$$p = \sqrt{\frac{\sqrt{\alpha^2+\beta^2}+\alpha}{2}} \qquad q = \sqrt{\frac{\sqrt{\alpha^2+\beta^2}-\alpha}{2}} \qquad \text{(Eq. 3)}$$

α and β are functions of frequency and are determined by the linearization of the dendritic nonlinearities as explained in Goldberg et al. (2007) and Remme and Rinzel (2011), with a negative amplifying parameter, μ_n, and a positive resonance parameter, μ_h (See Appendix 1).

$$\alpha(f) = \gamma_R + \frac{\mu_n}{1+(2\pi f\tau_n)^2} + \frac{\mu_h}{1+(2\pi f\tau_h)^2} \qquad \text{(Eq. 4a)}$$

$$\beta(f) = 2\pi f\left[\tau - \frac{\mu_n\tau_n}{1+(2\pi f\tau_n)^2} - \frac{\mu_h\tau_h}{1+(2\pi f\tau_h)^2}\right] \qquad \text{(Eq. 4b)}$$

Additional parameters include total dendritic conductance (relative to leak), γ_R, the membrane time constant τ, and the time constants representing the kinetics of the nonlinear dendritic conductances, as explained in Goldberg et al. (2007) and in Remme and Rinzel (2011). In some cases we only used the amplifying parameter in the fit (e.g., Figure 1C), and in Figure 3C, we used a Eq. 2 in the case of a passive dendrite for which $\alpha(f) = 1$ and $\beta(f) = 2\pi f\tau$.

Using the same formalism it is easy to show that for the (isopotential) soma with a quasi-linear membrane the phase delay is given by $\phi_s = \frac{1}{2\pi}\tan^{-1}\frac{\beta}{\alpha}$ (Eq. 5)

corresponding to an amplitude that is equal to $(\alpha^2 + \beta^2)^{-1/2}$ up to a scaling factor. In the main text, we point out that when μ_n becomes less negative ϕ_s is reduced. This is because when μ_n becomes less negative, α is increased (Eq. 4a) and β is decreased (Eq. 4b).

The amplitude attenuation and phase delays generated by the ChR2 kinetics are calculated from the Fourier transform of the alpha function (Eq. 1) and are given by

$$A_C(f) \propto \{(1 - \tau_r\tau_d(2\pi f)^2)^2 + (2\pi f[\tau_r + \tau_d])^2\}^{-1/2} \quad \text{(Eq. 6a)}$$

$$\phi_C(f) = \frac{1}{2\pi}\tan^{-1}\left(\frac{2\pi f[\tau_r + \tau_d]}{1 - \tau_r\tau_d(2\pi f)^2}\right) \quad \text{(Eq. 6b)}$$

Acknowledgments

This work was funded by a European Research Council (ERC) Consolidator Grant (no. 646886) to J.A.G. and grants from the Israel Science Foundation (no. 2051/20), German Research Foundation (CRC TRR295), Israel-China Binational Science Foundation and the Silverstein Foundation to H.B. We would like to thank Ronit Cherki, Tamar Licht and Anatoly Shapochnikov for excellent technical assistance.

Competing interests

The authors declare no competing interests.

References

Abudukeyoumu N, Hernandez-Flores T, Garcia-Munoz M, Arbuthnott GW. 2019. Cholinergic modulation of striatal microcircuits. *Eur J Neurosci* **49**:604–622. doi:10.1111/ejn.13949

Aceves Buendia J de J, Tiroshi L, Chiu W, Goldberg JA. 2019. Selective remodeling of glutamatergic transmission to striatal cholinergic interneurons after dopamine depletion. *Eur J Neurosci* **49**:824–833. doi:10.1111/ejn.13715

Alzheimer C, Schwindt P, Crill W. 1993. Modal gating of Na+ channels as a mechanism of persistent Na+ current in pyramidal neurons from rat and cat sensorimotor cortex. *J Neurosci* **13**:660–673. doi:10.1523/JNEUROSCI.13-02-00660.1993

Aoki S, Liu AW, Akamine Y, Zucca A, Zucca S, Wickens JR. 2018. Cholinergic interneurons in the rat striatum modulate substitution of habits. *Eur J Neurosci* **47**:1194–1205. doi:10.1111/ejn.13820

Aosaki T, Kimura M, Graybiel AM. 1995. Temporal and spatial characteristics of tonically active neurons of the primate's striatum. *J Neurophysiol* **73**:1234–1252.

Aosaki T, Tsubokawa H, Ishida A, Watanabe K, Graybiel AM, Kimura M. 1994. Responses of tonically active neurons in the primate's striatum undergo systematic changes during behavioral sensorimotor conditioning. *J Neurosci* **14**:3969–3984.

Apicella P, Scarnati E, Schultz W. 1991. Tonically discharging neurons of monkey striatum respond to preparatory and rewarding stimuli. *Exp Brain Res* **84**:672–675.

Arenkiel BR, Peca J, Davison IG, Feliciano C, Deisseroth K, Augustine GJ, Ehlers MD, Feng G. 2007. In vivo light-induced activation of neural circuitry in transgenic mice expressing channelrhodopsin-2. *Neuron* **54**:205–218. doi:10.1016/j.neuron.2007.03.005

Assous M. 2021. Striatal cholinergic transmission. Focus on nicotinic receptors' influence in striatal circuits. *Eur J Neurosci* **53**:2421–2442. doi:10.1111/ejn.15135

Assous M, Dautan D, Tepper JM, Mena-Segovia J. 2019. Pedunculopontine Glutamatergic Neurons Provide a Novel Source of Feedforward Inhibition in the Striatum by Selectively Targeting Interneurons. *J Neurosci* **39**:4727–4737. doi:10.1523/JNEUROSCI.2913-18.2019

Assous M, Kaminer J, Shah F, Garg A, Koós T, Tepper JM. 2017. Differential processing of thalamic information via distinct striatal interneuron circuits. *Nature Communications* **8**:15860. doi:10.1038/ncomms15860

Beatty Joseph A., Song SC, Wilson CJ. 2015. Cell-type-specific resonances shape the responses of striatal neurons to synaptic input. *Journal of Neurophysiology* **113**:688–700. doi:10.1152/jn.00827.2014

Bennett BD, Callaway JC, Wilson CJ. 2000. Intrinsic membrane properties underlying spontaneous tonic firing in neostriatal cholinergic interneurons. *J Neurosci* **20**:8493–8503. doi:20/22/8493 [pii]

Bennett BD, Wilson CJ. 1999. Spontaneous activity of neostriatal cholinergic interneurons in vitro. *J Neurosci* **19**:5586–5596.

Berger T, Larkum ME, Lüscher H-R. 2001. High I_h Channel Density in the Distal Apical Dendrite of Layer V Pyramidal Cells Increases Bidirectional Attenuation of EPSPs. *Journal of Neurophysiology* **85**:855–868. doi:10.1152/jn.2001.85.2.855

Bradfield LA, Bertran-Gonzalez J, Chieng B, Balleine BW. 2013. The Thalamostriatal Pathway and Cholinergic Control of Goal-Directed Action: Interlacing New with Existing Learning in the Striatum. *Neuron* **79**:153–166. doi:10.1016/j.neuron.2013.04.039

Brown RE, Basheer R, McKenna JT, Strecker RE, McCarley RW. 2012. Control of Sleep and Wakefulness. *Physiological Reviews* **92**:1087–1187. doi:10.1152/physrev.00032.2011

Buzsáki G, Anastassiou CA, Koch C. 2012. The origin of extracellular fields and currents — EEG, ECoG, LFP and spikes. *Nat Rev Neurosci* **13**:407–420. doi:10.1038/nrn3241

Carter AG, Sabatini BL. 2004. State-Dependent Calcium Signaling in Dendritic Spines of Striatal Medium Spiny Neurons. *Neuron* **44**:483–493. doi:10.1016/j.neuron.2004.10.013

Choi SJ, Ma TC, Ding Y, Cheung T, Joshi N, Sulzer D, Mosharov EV, Kang UJ. 2020. Alterations in the intrinsic properties of striatal cholinergic interneurons after dopamine lesion and chronic L-DOPA. *eLife* **9**:e56920. doi:10.7554/eLife.56920

Day M, Wokosin D, Plotkin JL, Tian X, Surmeier DJ. 2008. Differential Excitability and Modulation of Striatal Medium Spiny Neuron Dendrites. *Journal of Neuroscience* **28**:11603–11614. doi:10.1523/JNEUROSCI.1840-08.2008

Deng P, Zhang Y, Xu ZC. 2007. Involvement of I(h) in dopamine modulation of tonic firing in striatal cholinergic interneurons. *J Neurosci* **27**:3148–3156. doi:27/12/3148 [pii] 10.1523/JNEUROSCI.5535-06.2007

Deng YP, Wong T, Bricker-Anthony C, Deng B, Reiner A. 2013. Loss of corticostriatal and thalamostriatal synaptic terminals precedes striatal projection neuron pathology in heterozygous Q140 Huntington's disease mice. *Neurobiol Dis* **60**:89–107. doi:10.1016/j.nbd.2013.08.009

Ding J, Guzman JN, Tkatch T, Chen S, Goldberg JA, Ebert PJ, Levitt P, Wilson CJ, Hamm HE, Surmeier DJ. 2006. RGS4-dependent attenuation of M4 autoreceptor function in striatal cholinergic interneurons following dopamine depletion. *Nat Neurosci* **9**:832–842. doi:10.1038/nn1700

Ding JB, Guzman JN, Peterson JD, Goldberg JA, Surmeier DJ. 2010. Thalamic Gating of Corticostriatal Signaling by Cholinergic Interneurons. *Neuron* **67**:294–307. doi:10.1016/j.neuron.2010.06.017

Ding Y, Won L, Britt JP, Lim SAO, McGehee DS, Kang UJ. 2011. Enhanced striatal cholinergic neuronal activity mediates L-DOPA-induced dyskinesia in parkinsonian mice. *Proceedings of the National Academy of Sciences* **108**:840–845. doi:10.1073/pnas.1006511108

Doig NM, Magill PJ, Apicella P, Bolam JP, Sharott A. 2014. Cortical and Thalamic Excitation Mediate the Multiphasic Responses of Striatal Cholinergic Interneurons to Motivationally Salient Stimuli. *Journal of Neuroscience* **34**:3101–3117. doi:10.1523/JNEUROSCI.4627-13.2014

Ermentrout B. 2002. Simulating, Analyzing, and Animating Dynamical Systems: A Guide to XPPAUT for Researchers and Students. Philadelphia: Society for Industrial and Applied Mathematics.

Eskow Jaunarajs KL, Bonsi P, Chesselet MF, Standaert DG, Pisani A. 2015. Striatal cholinergic dysfunction as a unifying theme in the pathophysiology of dystonia. *Progress in Neurobiology* **127–128**:91–107. doi:10.1016/j.pneurobio.2015.02.002

Goldberg JA, Deister CA, Wilson CJ. 2007. Response Properties and Synchronization of Rhythmically Firing Dendritic Neurons. *Journal of Neurophysiology* **97**:208–219. doi:10.1152/jn.00810.2006

Goldberg JA, Ding JB, Surmeier DJ. 2012. Muscarinic Modulation of Striatal Function and Circuitry In: Fryer AD, Christopoulos A, Nathanson NM, editors. Muscarinic Receptors, Handbook of Experimental Pharmacology. Berlin, Heidelberg: Springer Berlin Heidelberg. pp. 223–241. doi:10.1007/978-3-642-23274-9_10

Goldberg JA, Kats SS, Jaeger D. 2003. Globus Pallidus Discharge Is Coincident with Striatal Activity during Global Slow Wave Activity in the Rat. *J Neurosci* **23**:10058–10063. doi:10.1523/JNEUROSCI.23-31-10058.2003

Goldberg JA, Reynolds JN. 2011. Spontaneous firing and evoked pauses in the tonically active cholinergic interneurons of the striatum. *Neuroscience* **198**:27–43. doi:10.1016/j.neuroscience.2011.08.067

Goldberg JA, Teagarden MA, Foehring RC, Wilson CJ. 2009. Nonequilibrium Calcium Dynamics Regulate the Autonomous Firing Pattern of Rat Striatal Cholinergic Interneurons. *Journal of Neuroscience* **29**:8396–8407. doi:10.1523/JNEUROSCI.5582-08.2009

Goldberg JA, Wilson CJ. 2010. The Cholinergic Interneurons of the Striatum: Intrinsic Properties Underlie Multiple Discharge Patterns. In: Steiner H, Tseng KY, editors.

Handbook of Basal Ganglia Structure and Function. London: Academic Press. pp. 133–149.

Goldberg JA, Wilson CJ. 2005. Control of Spontaneous Firing Patterns by the Selective Coupling of Calcium Currents to Calcium-Activated Potassium Currents in Striatal Cholinergic Interneurons. *Journal of Neuroscience* **25**:10230–10238. doi:10.1523/JNEUROSCI.2734-05.2005

Gradinaru V, Mogri M, Thompson KR, Henderson JM, Deisseroth K. 2009. Optical deconstruction of parkinsonian neural circuitry. *Science* **324**:354–359. doi:10.1126/science.1167093

Graybiel A, Aosaki T, Flaherty A, Kimura M. 1994. The basal ganglia and adaptive motor control. *Science* **265**:1826–1831. doi:10.1126/science.8091209

Gritton HJ, Howe WM, Romano MF, DiFeliceantonio AG, Kramer MA, Saligrama V, Bucklin ME, Zemel D, Han X. 2019. Unique contributions of parvalbumin and cholinergic interneurons in organizing striatal networks during movement. *Nat Neurosci* **22**:586–597. doi:10.1038/s41593-019-0341-3

Harnett MT, Magee JC, Williams SR. 2015. Distribution and Function of HCN Channels in the Apical Dendritic Tuft of Neocortical Pyramidal Neurons. *Journal of Neuroscience* **35**:1024–1037. doi:10.1523/JNEUROSCI.2813-14.2015

Häusser M. 2021. Optogenetics — The Might of Light. *N Engl J Med* **385**:1623–1626. doi:10.1056/NEJMcibr2111915

Helseth AR, Hernandez-Martinez R, Hall VL, Oliver ML, Turner BD, Caffall ZF, Rittiner JE, Shipman MK, King CS, Gradinaru V, Gerfen C, Costa-Mattioli M, Calakos N. 2021. Cholinergic neurons constitutively engage the ISR for dopamine modulation and skill learning in mice. *Science* **372**:eabe1931. doi:10.1126/science.abe1931

Higgs MH, Wilson CJ. 2017. Measurement of phase resetting curves using optogenetic barrage stimuli. *Journal of Neuroscience Methods* **289**:23–30. doi:10.1016/j.jneumeth.2017.06.018

Howe M, Ridouh I, Allegra Mascaro AL, Larios A, Azcorra M, Dombeck DA. 2019. Coordination of rapid cholinergic and dopaminergic signaling in striatum during spontaneous movement. *eLife* **8**:e44903. doi:10.7554/eLife.44903

Hutcheon B, Miura RM, Puil E. 1996. Subthreshold membrane resonance in neocortical neurons. *Journal of Neurophysiology* **76**:683–697. doi:10.1152/jn.1996.76.2.683

Hutcheon B, Yarom Y. 2000. Resonance, oscillation and the intrinsic frequency preferences of neurons. *Trends in Neurosciences* **23**:216–222. doi:10.1016/S0166-2236(00)01547-2

Johansson Y, Silberberg G. 2020. The Functional Organization of Cortical and Thalamic Inputs onto Five Types of Striatal Neurons Is Determined by Source and Target Cell Identities. *Cell Reports* **30**:1178-1194.e3. doi:10.1016/j.celrep.2019.12.095

Joshua M, Adler A, Mitelman R, Vaadia E, Bergman H. 2008. Midbrain Dopaminergic Neurons and Striatal Cholinergic Interneurons Encode the Difference between Reward and Aversive Events at Different Epochs of Probabilistic Classical Conditioning Trials. *Journal of Neuroscience* **28**:11673–11684. doi:10.1523/JNEUROSCI.3839-08.2008

Kawaguchi Y. 1993. Physiological, morphological, and histochemical characterization of three classes of interneurons in rat neostriatum. *J Neurosci* **13**:4908–4923. doi:10.1523/JNEUROSCI.13-11-04908.1993

Kerr JND. 2004. Action Potential Timing Determines Dendritic Calcium during Striatal Up-States. *Journal of Neuroscience* **24**:877–885. doi:10.1523/JNEUROSCI.4475-03.2004

Kim CK, Adhikari A, Deisseroth K. 2017. Integration of optogenetics with complementary methodologies in systems neuroscience. *Nat Rev Neurosci* **18**:222–235. doi:10.1038/nrn.2017.15

Kimura M, Rajkowski J, Evarts E. 1984. Tonically discharging putamen neurons exhibit set-dependent responses. *Proceedings of the National Academy of Sciences* **81**:4998–5001. doi:10.1073/pnas.81.15.4998

Koch C. 1984. Cable theory in neurons with active, linearized membranes. *Biol Cybern* **50**:15–33. doi:10.1007/BF00317936

Kole MHP, Hallermann S, Stuart GJ. 2006. Single I_h Channels in Pyramidal Neuron Dendrites: Properties, Distribution, and Impact on Action Potential Output. *J Neurosci* **26**:1677–1687. doi:10.1523/JNEUROSCI.3664-05.2006

Kosillo P, Zhang Y-F, Threlfell S, Cragg SJ. 2016. Cortical Control of Striatal Dopamine Transmission via Striatal Cholinergic Interneurons. *Cereb Cortex* **26**:4160–4169. doi:10.1093/cercor/bhw252

Lapper SR, Bolam JP. 1992. Input From the Frontal Cortex and the Nucleus To Cholinergic Interneurons in the Dorsal of the Rat **51**:533–545.

Liu D, Dan Y. 2019. A Motor Theory of Sleep-Wake Control: Arousal-Action Circuit. *Annu Rev Neurosci* **42**:27–46. doi:10.1146/annurev-neuro-080317-061813

Mahon S. 2001. Relationship between EEG Potentials and Intracellular Activity of Striatal and Cortico-striatal Neurons: an In Vivo Study under Different Anesthetics. *Cerebral Cortex* **11**:360–373. doi:10.1093/cercor/11.4.360

Mallet N, Leblois A, Maurice N, Beurrier C. 2019. Striatal Cholinergic Interneurons: How to Elucidate Their Function in Health and Disease. *Front Pharmacol* **10**:1488. doi:10.3389/fphar.2019.01488

Mamaligas AA, Barcomb K, Ford CP. 2019. Cholinergic Transmission at Muscarinic Synapses in the Striatum Is Driven Equally by Cortical and Thalamic Inputs. *Cell Reports* **28**:1003-1014.e3. doi:10.1016/j.celrep.2019.06.077

Martin RF, Bowden DM. 2000. Primate brain maps: structure of the macaque brain. Elsevier.

Matityahu L, Malgady JM, Schirelman M, Johansson Y, Wilking JA, Silberberg G, Goldberg JA, Plotkin JL. 2022. A tonic nicotinic brake controls spike timing in striatal spiny projection neurons. *eLife* **11**:e75829. doi:10.7554/eLife.75829

Matsumoto N, Minamimoto T, Graybiel AM, Kimura M. 2001. Neurons in the Thalamic CM-Pf Complex Supply Striatal Neurons With Information About Behaviorally Significant Sensory Events. *Journal of Neurophysiology* **85**:960–976. doi:10.1152/jn.2001.85.2.960

Maurice N. 2004. D2 Dopamine Receptor-Mediated Modulation of Voltage-Dependent Na+ Channels Reduces Autonomous Activity in Striatal Cholinergic Interneurons. *Journal of Neuroscience* **24**:10289–10301. doi:10.1523/JNEUROSCI.2155-04.2004

Mauro A, Conti F, Dodge F, Schor R. 1970. Subthreshold Behavior and Phenomenological Impedance of the Squid Giant Axon. *Journal of General Physiology* **55**:497–523. doi:10.1085/jgp.55.4.497

McGuirt AF, Post MR, Pigulevskiy I, Sulzer D, Lieberman OJ. 2021. Coordinated Postnatal Maturation of Striatal Cholinergic Interneurons and Dopamine Release Dynamics in Mice. *J Neurosci* **41**:3597–3609. doi:10.1523/JNEUROSCI.0755-20.2021

Mizrahi-Kliger AD, Kaplan A, Israel Z, Bergman H. 2018. Desynchronization of slow oscillations in the basal ganglia during natural sleep. *Proc Natl Acad Sci USA* **115**:E4274–E4283. doi:10.1073/pnas.1720795115

Morris G, Arkadir D, Nevet A, Vaadia E, Bergman H. 2004. Coincident but distinct messages of midbrain dopamine and striatal tonically active neurons. *Neuron* **43**:133–143. doi:10.1016/j.neuron.2004.06.012 S0896627304003551 [pii]

Nagel G, Szellas T, Huhn W, Kateriya S, Adeishvili N, Berthold P, Ollig D, Hegemann P, Bamberg E. 2003. Channelrhodopsin-2, a directly light-gated cation-selective membrane channel. *Proc Natl Acad Sci USA* **100**:13940–13945. doi:10.1073/pnas.1936192100

Oswald MJ, Oorschot DE, Schulz JM, Lipski J, Reynolds JN. 2009. IH current generates the afterhyperpolarisation following activation of subthreshold cortical synaptic inputs to striatal cholinergic interneurons. *J Physiol* **587**:5879–5897. doi:jphysiol.2009.177600 [pii] 10.1113/jphysiol.2009.177600

Parker PRL, Lalive AL, Kreitzer AC. 2016. Pathway-Specific Remodeling of Thalamostriatal Synapses in Parkinsonian Mice. *Neuron* **89**:734–740. doi:10.1016/j.neuron.2015.12.038

Paz RM, Tubert C, Stahl AM, Amarillo Y, Rela L, Murer MG. 2021. Levodopa Causes Striatal Cholinergic Interneuron Burst-Pause Activity in Parkinsonian Mice. *Mov Disord* **36**:1578–1591. doi:10.1002/mds.28516

Petreanu L, Mao T, Sternson SM, Svoboda K. 2009. The subcellular organization of neocortical excitatory connections. *Nature* **457**:1142–5. doi:10.1038/nature07709

Pisani A, Bernardi G, Ding J, Surmeier DJ. 2007. Re-emergence of striatal cholinergic interneurons in movement disorders. *Trends in Neurosciences* **30**:545–553. doi:10.1016/j.tins.2007.07.008

Plotkin JL, Day M, Surmeier DJ. 2011. Synaptically driven state transitions in distal dendrites of striatal spiny neurons. *Nat Neurosci* **14**:881–888. doi:10.1038/nn.2848

Plotkin JL, Goldberg JA. 2019. Thinking Outside the Box (and Arrow): Current Themes in Striatal Dysfunction in Movement Disorders. *Neuroscientist* **25**:359–379. doi:10.1177/1073858418807887

Poppi LA, Ho-Nguyen KT, Shi A, Daut CT, Tischfield MA. 2021. Recurrent Implication of Striatal Cholinergic Interneurons in a Range of Neurodevelopmental, Neurodegenerative, and Neuropsychiatric Disorders. *Cells* **10**:907. doi:10.3390/cells10040907

Raz A, Feingold A, Zelanskaya V, Vaadia E, Bergman H. 1996. Neuronal synchronization of tonically active neurons in the striatum of normal and parkinsonian primates. *J Neurophysiol* **76**:2083–2088.

Rehani R, Atamna Y, Tiroshi L, Chiu W-H, de Jesús Aceves Buendía J, Martins GJ, Jacobson GA, Goldberg JA. 2019. Activity Patterns in the Neuropil of Striatal Cholinergic Interneurons in Freely Moving Mice Represent Their Collective Spiking Dynamics. *eNeuro* **6**:ENEURO.0351-18.2018. doi:10.1523/ENEURO.0351-18.2018

Reig R, Silberberg G. 2014. Multisensory Integration in the Mouse Striatum. *Neuron* **83**:1200–1212. doi:10.1016/j.neuron.2014.07.033

Remme MWH, Rinzel J. 2011. Role of active dendritic conductances in subthreshold input integration. *J Comput Neurosci* **31**:13–30. doi:10.1007/s10827-010-0295-7

Riedner BA, Vyazovskiy VV, Huber R, Massimini M, Esser S, Murphy M, Tononi G. 2007. Sleep Homeostasis and Cortical Synchronization: III. A High-Density EEG Study of Sleep Slow Waves in Humans. *Sleep* **30**:1643–1657. doi:10.1093/sleep/30.12.1643

Schulz JM, Oswald MJ, Reynolds JNJ. 2011. Visual-Induced Excitation Leads to Firing Pauses in Striatal Cholinergic Interneurons. *Journal of Neuroscience* **31**:11133–11143. doi:10.1523/JNEUROSCI.0661-11.2011

Schulz JM, Reynolds JNJ. 2013. Pause and rebound: sensory control of cholinergic signaling in the striatum. *Trends in Neurosciences* **36**:41–50. doi:10.1016/j.tins.2012.09.006

Sela Y, Vyazovskiy VV, Cirelli C, Tononi G, Nir Y. 2016. Responses in Rat Core Auditory Cortex are Preserved during Sleep Spindle Oscillations. *Sleep* **39**:1069–1082. doi:10.5665/sleep.5758

1078 Sharott A, Doig NM, Mallet N, Magill PJ. 2012. Relationships between the Firing of
1079 Identified Striatal Interneurons and Spontaneous and Driven Cortical Activities In
1080 Vivo. *Journal of Neuroscience* **32**:13221–13236. doi:10.1523/JNEUROSCI.2440-
1081 12.2012
1082 Smith Y, Raju DV, Pare JF, Sidibe M. 2004. The thalamostriatal system: a highly specific
1083 network of the basal ganglia circuitry. *Trends Neurosci* **27**:520–527.
1084 doi:10.1016/j.tins.2004.07.004 S0166-2236(04)00232-2 [pii]
1085 Song WJ, Surmeier DJ. 1996. Voltage-dependent facilitation of calcium channels in rat
1086 neostriatal neurons. *J Neurophysiol* **76**:2290–2306.
1087 Stern EA, Jaeger D, Wilson CJ. 1998. Membrane potential synchrony of simultaneously
1088 recorded striatal spiny neurons in vivo. *Nature* **394**:475–478. doi:10.1038/28848
1089 Tanimura A, Du Y, Kondapalli J, Wokosin DL, Surmeier DJ. 2019. Cholinergic Interneurons
1090 Amplify Thalamostriatal Excitation of Striatal Indirect Pathway Neurons in
1091 Parkinson's Disease Models. *Neuron* **101**:444-458.e6.
1092 doi:10.1016/j.neuron.2018.12.004
1093 Tanimura A, Lim SAO, Aceves Buendia J de J, Goldberg JA, Surmeier DJ. 2016.
1094 Cholinergic Interneurons Amplify Corticostriatal Synaptic Responses in the Q175
1095 Model of Huntington's Disease. *Front Syst Neurosci* **10**.
1096 doi:10.3389/fnsys.2016.00102
1097 Tchumatchenko T, Newman JP, Fong M, Potter SM. 2013. Delivery of continuously-varying
1098 stimuli using channelrhodopsin-2. *Front Neural Circuits* **7**.
1099 doi:10.3389/fncir.2013.00184
1100 Thomas TM, Smith Y, Levey AI, Hersch SM. 2000. Cortical Inputs to m2-Immunoreactive
1101 Striatal Interneurons in Rat and Monkey. *Synapse* **37**:252–261.
1102 Thorn CA, Graybiel AM. 2010. Pausing to Regroup: Thalamic Gating of Cortico-Basal
1103 Ganglia Networks. *Neuron* **67**:175–178. doi:10.1016/j.neuron.2010.07.010
1104 Threlfell S, Lalic T, Platt NJ, Jennings KA, Deisseroth K, Cragg SJ. 2012. Striatal Dopamine
1105 Release Is Triggered by Synchronized Activity in Cholinergic Interneurons. *Neuron*
1106 **75**:58–64. doi:10.1016/j.neuron.2012.04.038
1107 Tiroshi L, Goldberg JA. 2019. Population dynamics and entrainment of basal ganglia
1108 pacemakers are shaped by their dendritic arbors. *PLoS Comput Biol* **15**:e1006782.
1109 doi:10.1371/journal.pcbi.1006782
1110 Tubert C, Murer MG. 2021. What's wrong with the striatal cholinergic interneurons in
1111 Parkinson's disease? Focus on intrinsic excitability. *Eur J Neurosci* **53**:2100–2116.
1112 doi:10.1111/ejn.14742
1113 Ulrich D. 2002. Dendritic Resonance in Rat Neocortical Pyramidal Cells. *Journal of*
1114 *Neurophysiology* **87**:2753–2759. doi:10.1152/jn.2002.87.6.2753
1115 Wilson C, Chang H, Kitai S. 1990. Firing patterns and synaptic potentials of identified giant
1116 aspiny interneurons in the rat neostriatum. *J Neurosci* **10**:508–519.
1117 doi:10.1523/JNEUROSCI.10-02-00508.1990
1118 Wilson CJ. 2005. The mechanism of intrinsic amplification of hyperpolarizations and
1119 spontaneous bursting in striatal cholinergic interneurons. *Neuron* **45**:575–585.
1120 Wilson CJ. 2004. Basal Ganglia In: Shepherd GM, editor. The Synaptic Organization of the
1121 Brain. New York: Oxford University Press. pp. 361–413.
1122 Wilson CJ, Goldberg JA. 2006. Origin of the slow afterhyperpolarization and slow rhythmic
1123 bursting in striatal cholinergic interneurons. *J Neurophysiol* **95**:196–204.
1124 doi:00630.2005 [pii] 10.1152/jn.00630.2005
1125 Yamanaka K, Hori Y, Minamimoto T, Yamada H, Matsumoto N, Enomoto K, Aosaki T,
1126 Graybiel AM, Kimura M. 2018. Roles of centromedian parafascicular nuclei of
1127 thalamus and cholinergic interneurons in the dorsal striatum in associative learning of

environmental events. *J Neural Transm* **125**:501–513. doi:10.1007/s00702-017-1713-z

Yarom O, Cohen D. 2011. Putative Cholinergic Interneurons in the Ventral and Dorsal Regions of the Striatum Have Distinct Roles in a Two Choice Alternative Association Task. *Front Syst Neurosci* **5**. doi:10.3389/fnsys.2011.00036